VETTAM: a scheme for radiation hydrodynamics with adaptive mesh refinement using the variable Eddington tensor method

Shyam H. Menon [ID],[1]★ Christoph Federrath [ID],[1,2] Mark R. Krumholz [ID],[1,2] Rolf Kuiper [ID],[3] Benjamin D. Wibking [ID][1,2] and Manuel Jung [ID][4]

[1]*Research School of Astronomy and Astrophysics, Australian National University, Canberra, ACT 2611, Australia*
[2]*ARC Centre of Excellence for Astronomy in Three Dimensions (ASTRO-3D), Canberra, ACT 2611, Australia*
[3]*Zentrum für Astronomie der Universität Heidelberg, Institut für Theoretische Astrophysik, Albert-Ueberle-Straße 2, D-69120 Heidelberg, Germany*
[4]*Hamburger Sternwarte, Universität Hamburg, Gojenbergsweg 112, D-21029 Hamburg, Germany*

ABSTRACT

We present Variable Eddington Tensor (VET)-closed Transport on Adaptive Meshes (VETTAM), a new algorithm to solve the equations of radiation hydrodynamics (RHD) with support for adaptive mesh refinement (AMR) in a frequency-integrated, two-moment formulation. The method is based on a non-local VET closure computed with a hybrid characteristics scheme for ray tracing. We use a Godunov method for the hyperbolic transport of radiation with an implicit backwards-Euler temporal update to avoid the explicit time-step constraint imposed by the light-crossing time, and a fixed-point Picard iteration scheme to handle the nonlinear gas-radiation exchange term, with the two implicit update stages jointly iterated to convergence. We also develop a modified wave-speed correction method for AMR, which we find to be crucial for obtaining accurate results in the diffusion regime. We demonstrate the robustness of our scheme with a suite of pure radiation and RHD tests, and show that it successfully captures the streaming, static diffusion, and dynamic diffusion regimes and the spatial transitions between them, casts sharp shadows, and yields accurate results for rates of momentum and energy exchange between radiation and gas. A comparison between different closures for the radiation moment equations, with the Eddington approximation (0th-moment closure) and the M_1 approximation (1st-moment closure), demonstrates the advantages of the VET method (2nd-moment closure) over the simpler closure schemes. VETTAM has been coupled to the AMR FLASH (magneto-)hydrodynamics code and we summarize by reporting performance features and bottlenecks of our implementation.

Key words: radiation mechanisms: thermal – radiative transfer – methods: numerical.

1 INTRODUCTION

Radiation hydrodynamics (RHD) plays a crucial role in the evolution of several astrophysical systems, such as stellar atmospheres (e.g. Mihalas 1978; Castor 2004), planetary atmospheres (e.g. Zhang 2020), stellar winds (e.g. Castor, Abbott & Klein 1975; Smith 2014), circumstellar discs (e.g. Turner et al. 2014; Zhao et al. 2020), supernovae (e.g. Janka et al. 2007), star-forming clouds in the interstellar medium (e.g. Krumholz, McKee & Bland-Hawthorn 2019; Rosen et al. 2020), active galactic nuclei and their associated jets (e.g. Davis & Tchekhovskoy 2020), and in galactic outflows (e.g. Naab & Ostriker 2017; Zhang 2018). These systems span a vast range of scales and physical conditions, which can be parametrized by the optical depth across the region of interest, determining how radiation is transported. While there exist various numerical techniques to solve the RHD equations in some limiting cases (e.g. high versus low optical depth), a crucial requirement of flexible modern methods is their ability to treat a mixture of regimes in a robust and efficient way.

There are well-known difficulties associated with numerically solving the RHD equations. The primary challenge has to do with the multidimensional nature of the radiation intensity – a function of spatial location, time, direction, and frequency – that effectively makes the radiative transfer (RT) equation very expensive to solve, especially in a dynamical system where this needs to be done multiple times (however, see Jiang 2021). A common approach to circumvent this is to integrate the RT equation over all frequencies and angles to obtain the grey radiation moment equations, reducing the dimensionality of the system (e.g. Pomraning 1973; Mihalas & Mihalas 1984; Castor 2004). However, this introduces the need for an extra closure equation to estimate the moments of the radiation intensity whose evolution is not explicitly computed. One commonly used closure is the flux-limited diffusion (FLD) method (e.g. Turner & Stone 2001; Howell & Greenough 2003; Krumholz et al. 2007a; Gittings et al. 2008; Swesty & Myra 2009; Kuiper et al. 2010; Commerçon et al. 2011; van der Holst et al. 2011; Zhang et al. 2011; Bitsch et al. 2013; Flock et al. 2013; Klassen et al. 2014; Ramsey & Dullemond 2015; Chatzopoulos & Weide 2019; Moens et al. 2021), which closes the equations at the first moment (the radiation flux), which is assumed to be proportional to the negative of the gradient in radiation energy density; this then implies that the Eddington tensor

★ E-mail: shyam.menon@anu.edu.au

is locally isotropic (Levermore & Pomraning 1981). The FLD closure reduces the radiation transport to a parabolic diffusion equation, with a diffusion coefficient chosen to limit the photon speed to be smaller than the speed of light. However, this method often suffers from inaccuracies in the optically thin regime, or when a mixture of low- and high-opacity gas is present. For instance, FLD methods cannot cast shadows (Hayes & Norman 2003; Kuiper & Klessen 2013).

A more accurate closure scheme that has recently been adopted widely is the M_1 closure (e.g. González, Audit & Huynh 2007; Aubert & Teyssier 2008; Rosdahl et al. 2013; Skinner & Ostriker 2013; Rosdahl & Teyssier 2015; Kannan et al. 2019; Skinner et al. 2019; Bloch et al. 2021; Chan et al. 2021; Melon Fuksman et al. 2021; Wibking & Krumholz 2021), which retains the time evolution of the radiation flux and adopts a local closure relation for the radiation pressure tensor, or equivalently the Eddington tensor, in terms of the local radiation energy density and flux; a variety of assumptions regarding the nature of the radiation field are possible, each yielding slightly different versions of the closure relation (Minerbo 1978; Levermore 1984). While the M_1 closure can handle transitions in optical depths for a single beam of radiation, it fails for other non-trivial geometrical distributions of radiation sources. For instance, the presence of multiple sources interacting in optically thin media causes un-physical discontinuities between the sources' radiation fronts, and produces spurious fluxes in the direction perpendicular to the line connecting the sources.

A more accurate alternative is the so-called variable eddington tensor (VET) scheme (e.g. Stone, Mihalas & Norman 1992; Gehmeyr & Mihalas 1994; Sekora & Stone 2010; Jiang, Stone & Davis 2012; Asahina, Takahashi & Ohsuga 2020), a non-local scheme that does not adopt a closure relation or model *a priori*, but rather computes the Eddington tensor self-consistently through a formal solution of the time-independent RT equation, along discrete rays using a ray-tracing approach (e.g. Davis, Stone & Jiang 2012). The self-consistently computed closure is combined with the radiation moment equations to solve for the radiation quantities. While more computationally expensive due to the required non-local ray-trace solution and its associated communication overheads, the VET approach does not face the shortcomings of the more approximate closure models discussed above. For example, the FLD and M_1 closure schemes can produce misleading results in some semitransparent problems (Krumholz & Thompson 2012; Kuiper & Klessen 2013; Rosdahl & Teyssier 2015; Kannan et al. 2019), and this was discovered only through a comparison of these simpler methods with a VET scheme (Davis et al. 2014) or other non-local closure schemes, such as a Monte Carlo approach (Harries 2015; Tsang & Milosavljević 2015; Smith et al. 2020).

Another difficulty associated with RHD is the vast difference in scale between the wave speeds associated with radiation and hydrodynamics – the speed of light (c) and gas flow speed (v)[1] in the medium, respectively. In many non-relativistic, astrophysical problems, $v/c \ll 1$, but stability constraints associated with explicit temporal updates restrict the time-step to the stringent radiation transport time-scale, which renders simulations that must follow the system for several hydrodynamical time-steps computationally infeasible. A popular approach to alleviate this issue is to adopt a reduced speed-of-light approximation (RSLA), wherein the speed of light is reduced to a fraction of its true value $\hat{c}$ (e.g. Gnedin & Abel 2001; Skinner & Ostriker 2013). This allows one to use an explicit temporal update

for the radiation quantities that is now limited by the much larger ratio $c_s/\hat{c}$. Explicit updates of the radiation moment equations with the RSLA have the advantage that they can adopt widely studied and well-tested tools for solving hyperbolic PDEs. These schemes are also, in general, well parallelizable and scalable, and can be accelerated with GPUs (Wibking & Krumholz 2021). However, the RSLA is only applicable under the condition that the hierarchy of evolution time-scales – namely the light crossing, radiation diffusion, and hydrodynamic time-scales – remains the same even with the reduced speed of light. This places constraints on the applicability of the RSLA in systems with high optical depth, the dynamic diffusion regime, limiting the overall flexibility of the scheme.

An alternative approach is to treat the transport of radiation at the hydrodynamic time-step in a fully implicit fashion to avoid stability-related issues. This approach has been used in a vast variety of implementations and has the benefit of being applicable in a broad range of systems. However, implicit methods require the solution of a large system of equations using sparse matrix solvers, whose performance and scalability are limited. This is aggravated by the presence of stiff, nonlinear terms that need to be handled implicitly, along with the radiation quantities, rendering the system of equations both non-local and nonlinear. However, implicit, non-local methods remain the gold standard of accuracy, and recent advancements in numerical methods, and the development of freely available and continually improving libraries of linear/nonlinear sparse matrix solvers using Krylov subspace methods, has accelerated the development of implicit RHD schemes that can be applied on massively parallel computing architectures (Saad 2003).

In this paper, we present VET-closed Transport on Adaptive Meshes (VETTAM),[2] the first multidimensional radiation moment scheme closed using a VET computed through a formal solution of the RT equation with adaptive mesh refinement (AMR) capabilities. The formal solution is computed through a method based on the hybrid characteristics ray-tracing implemented in Buntemeyer et al. (2016).[3] We couple this with the update of the radiation moment equations in a fully time-implicit fashion that can handle all regimes of optical depth in radiation transport. We solve the resulting implicit system of nonlinear equations with a fixed-point Picard iteration scheme that allows us to use a variety of sparse Krylov subspace matrix solvers provided with the PETSc library[4] (Balay et al. 1997, 2021). We describe our scheme, its salient features, and its integration into the FLASH code (Fryxell et al. 2000; Dubey, Reid & Fisher 2008) in Section 2. In Section 3, we present a comprehensive test suite to demonstrate the accuracy and capabilities of our algorithm. In Section 4, we discuss the advantages of our VET scheme over methods that adopt simpler closures, touch upon the performance capabilities of our scheme, and list some caveats associated with our implementation that provide scope for future improvements. We briefly summarize in Section 5 and mention potential applications for which we intend to use VETTAM in the near future.

2 NUMERICAL METHODOLOGY

In this section, we describe our implementation to treat the coupled RHD set of equations, fully integrated into the FLASH code (Fryxell

---

[1]For strongly subsonic flows, the relavant wavespeed for the timestep is the sound speed c_s.

[2]VETTAM is an acronym for VET closed Transport on Adaptive Meshes. The acronym stands for *light* in the south Indian language of Malayalam – the first language of SHM.

[3]The module has been rewritten and improved significantly by Manuel Jung.

[4]https://petsc.org/release/

et al. 2000; Dubey et al. 2008). FLASH is a publicly available high-performance general application (astro-)physics code that includes a wide range of physical capabilities and is designed in an organized modular fashion (Dubey, Tzeferacos & Lamb 2019). It solves the hydrodynamic equations on an Eulerian mesh, with AMR (Berger & Colella 1989) using the PARAMESH library (MacNeice et al. 2000). By default it uses a modified second derivative normalized by the average gradient of a chosen variable over a cell as a dimensionless criterion for refinement (Lohner 1987), although other refinement criteria are available or straightforward to implement (such as Jeans refinement Federrath et al. 2010).

2.1 Equations of radiation hydrodynamics

In VETTAM, we solve the equations of non-relativistic grey (frequency-integrated) RHD in conservative form, written in the mixed-frame formulation, i.e. where the moments of the radiation intensity are written in the lab frame, and the opacities are written in the comoving frame, with the transformation between the frames accounted by $\mathcal{O}(v/c)$ terms in the resulting equations (e.g. Mihalas & Klein 1982; Krumholz et al. 2007a). This approach takes advantage of the simplicity of the hyperbolic operators in the lab frame, and the simplicity of the matter emissivities and opacities in the comoving frame, where they are generally isotropic (see Castor 2009, for a detailed critique of these various approaches). An additional advantage is that the mixed-frame formulation permits conservation of total energy, whereas a comoving-frame formulation of the equations does not; this is especially important for AMR, where non-conservation may be amplified by repeated refinements. However, the $\mathcal{O}(v/c)$ expansions to transform the opacities in the mixed-frame equations fail for emission/absorption lines as soon as v/c becomes comparable to $\Delta\lambda/\lambda_0$, where $\Delta\lambda$ and λ_0 are the linewidth and line centre; this limits the use of the mixed-frame approach to broad lines or continuum radiation. Since we are interested in modelling dust continuum radiation with VETTAM on an AMR grid, the advantages of the mixed-frame formulation outweigh its disadvantages. In writing out the equations, we are careful to retain terms that are of leading order in all regimes of RHD, using the scalings for various terms given in table 1 of Krumholz et al. (2007a), to ensure that our scheme recovers the correct asymptotic limits (Lowrie, Morel & Hittinger 1999). We neglect scattering for simplicity; however, an extension to include scattering would be straightforward. Finally, we assume the matter is always in local thermodynamic equilibrium, though not necessarily in equilibrium with the radiation field, and we treat the material property coefficients as isotropic in the comoving frame.

We adopt the following convention to represent the RHD operations: tensor contractions over a single index with dots (e.g. $\boldsymbol{a} \cdot \boldsymbol{b}$), tensor contractions over two indices by colons (e.g. $\mathbf{a} : \mathbf{b}$), and tensor products of vectors without an operator symbol (e.g. $\boldsymbol{ab}$). The equations solved by VETTAM are then

$$\frac{\partial \rho}{\partial t} + \nabla \cdot (\rho \mathbf{v}) = 0 \tag{1}$$

$$\frac{\partial (\rho \mathbf{v})}{\partial t} + \nabla \cdot (\rho \mathbf{vv}) = -\nabla P - \rho \nabla \Phi + \boldsymbol{G} + \dot{\boldsymbol{p}}_* \tag{2}$$

$$\frac{\partial E}{\partial t} + \nabla \cdot [(E + P)\mathbf{v}] = -\rho \mathbf{v} \cdot \nabla \Phi + cG^0 + \dot{E}_* \tag{3}$$

$$\frac{\partial E_r}{\partial t} + \nabla \cdot \boldsymbol{F}_r = -cG^0 \tag{4}$$

$$\frac{\partial \boldsymbol{F}_r}{\partial t} + \nabla \cdot (c^2 E_r \mathbf{T}) = -c^2 \boldsymbol{G}, \tag{5}$$

where the pressure is given by the ideal gas law,

$$P = \frac{\rho k_{\mathrm{B}} T}{\mu}, \tag{6}$$

and

$$G^0 = \rho \kappa_E E_r - \rho \kappa_P a_R T^4 + \rho \left(\kappa_F - 2\kappa_E\right) \frac{\boldsymbol{v} \cdot \boldsymbol{F}_r}{c^2} \\ + \rho \left(\kappa_E - \kappa_F\right) \left[\frac{v^2}{c^2} E_r + \frac{\boldsymbol{vv}}{c^2} : \mathbf{P}_r\right], \tag{7}$$

and

$$\boldsymbol{G} = \rho \kappa_R \frac{\boldsymbol{F}_r}{c} - \rho \kappa_R E_r \frac{\boldsymbol{v}}{c} \cdot (\mathbf{I} + \mathbf{T}), \tag{8}$$

are the time-like and space-like parts of the specific radiation four-force density for a direction-independent flux spectrum (Mihalas & Auer 2001) to leading order in all regimes. In the above equations ρ is the mass density, P the gas thermal pressure, $\boldsymbol{v}$ the gas velocity, Φ the gravitational potential, T the gas temperature, $\mathbf{I}$ the identity matrix, and c the speed of light in vacuum. E is the total gas energy density, given by

$$E = E_g + \frac{1}{2} \rho v^2, \tag{9}$$

where E_g is the gas internal energy density. In the ideal gas law, equation (6), k_{B} is the Boltzmann constant and μ the mean particle mass. As for the radiation quantities, E_r is the lab-frame radiation energy density, $\boldsymbol{F}_r$ the lab-frame radiation momentum density, $\mathbf{P}_r$ is the lab-frame radiation pressure tensor, and a_R the radiation constant. The radiation moment quantities are related to the radiation intensity $I_r(\hat{\boldsymbol{n}}_k, \nu)$ travelling in direction $\hat{\boldsymbol{n}}_k$ by the relations

$$cE_r = \int_0^\infty d\nu \int d\Omega \, I_r(\hat{\boldsymbol{n}}_k, \nu) \tag{10}$$

$$\boldsymbol{F}_r = \int_0^\infty d\nu \int d\Omega \, \hat{\boldsymbol{n}}_k \, I_r(\hat{\boldsymbol{n}}_k, \nu) \tag{11}$$

$$c\mathbf{P}_r = \int_0^\infty d\nu \int d\Omega \, \hat{\boldsymbol{n}}_k \hat{\boldsymbol{n}}_k \, I_r(\hat{\boldsymbol{n}}_k, \nu), \tag{12}$$

where $d\Omega$ and $d\nu$ are the infinitesimal solid angle and lab-frame frequencies, respectively. The radiation closure relation is used to close the above system of equations, and is of the form

$$\mathbf{P}_r = \mathbf{T} E_r, \tag{13}$$

where $\mathbf{T}$ is the Eddington Tensor. We use an Eddington tensor directly calculated from angular quadratures of the frequency-averaged specific intensity $I_r(\hat{\boldsymbol{n}}_k)$, using relations (10) and (12), where I_r as a function of the spatial path-length s is calculated from a formal solution of the time-independent RT equation

$$\frac{\partial I_r}{\partial s} = \rho \kappa (S - I_r), \tag{14}$$

where S is the source function, which, for the purposes of modelling the emission from dust grains, we set equal to the frequency-integrated Planck function $B(T) = ca_R T^4/(4\pi)$. The expression in equation (14) neglects scattering, and assumes that the dust emits and absorbs radiation in the comoving frame with the same grey opacity $\kappa = \int_0^\infty \kappa(\nu_0) d\nu_0$, where $\kappa(\nu_0)$ is the material opacity at frequency ν_0. In addition, we also ignore $\mathcal{O}(v/c)$ terms in this equation, which arise from the mixed-frame formulation, since we expect the contribution of these terms to the Eddington tensor to

be relatively low. $\dot{E}_*$ and $\dot{\boldsymbol{p}}_*$ denote the energy and momentum deposition rates to the gas by the direct radiation from point sources or sink particles (Federrath et al. 2010). We split this direct contribution from the diffuse radiation modelled by the VET, and treat it directly, using only a ray tracer on rays originating at the sources[5] (Wolfire & Cassinelli 1986; Murray et al. 1994; Kuiper et al. 2010; Bitsch et al. 2013; Flock et al. 2013; Kolb et al. 2013; Klassen et al. 2014; Ramsey & Dullemond 2015; Rosen et al. 2017; Mignon-Risse et al. 2020). We provide further details on these terms in Section 2.2.6.

The material coefficients κ_P, κ_E, and κ_F are the Planck-mean, energy-mean, and flux-mean frequency-integrated specific opacities evaluated in the comoving frame, and are given by,

$$\kappa_P \equiv \frac{\int_0^\infty \kappa(v_0)\,B(v_0, T)\,dv_0}{\int_0^\infty B(v_0, T)dv_0}, \tag{15}$$

$$\kappa_E \equiv \frac{\int_0^\infty \kappa(v_0)\,E_{r0}(v_0)\,dv_0}{\int_0^\infty E_{r0}(v_0)dv_0}, \tag{16}$$

$$\kappa_F \equiv \frac{\int_0^\infty \kappa(v_0)\,\boldsymbol{F}_{r0}(v_0)\,dv_0}{\int_0^\infty \boldsymbol{F}_{r0}(v_0)dv_0}, \tag{17}$$

where $B(v_0, T)$ is the frequency-dependent Planck function, $E_{r0}(v_0)$ the radiation energy density per unit frequency, and $\boldsymbol{F}_{r0}(v_0)$ the radiation flux per unit frequency, all defined in the comoving frame. The lab-frame and comoving-frame quantities are related by (e.g. Castor 2004)

$$E_r = E_{r0} + 2\frac{\boldsymbol{v} \cdot \boldsymbol{F}_{r0}}{c^2} + \frac{1}{c^2}\left[v^2 E_{r0} + (\boldsymbol{v}\boldsymbol{v}) : \mathbf{P}_{r0}\right], \tag{18}$$

$$\boldsymbol{F}_r = \boldsymbol{F}_{r0} + \boldsymbol{v}E_0 + \boldsymbol{v} \cdot \mathbf{P}_{r0} + \frac{1}{2c^2}\left[v^2 \boldsymbol{F}_{r0} + 3\boldsymbol{v}(\boldsymbol{v} \cdot \boldsymbol{F}_{r0})\right], \tag{19}$$

$$\mathbf{P}_r = \mathbf{P}_{r0} + \frac{\boldsymbol{v}\boldsymbol{F}_{r0} + \boldsymbol{F}_{r0}\boldsymbol{v}}{c^2} + \frac{1}{c^2}\left[\boldsymbol{v}\boldsymbol{v}E_{r0} + \boldsymbol{v}(\boldsymbol{v} \cdot \mathbf{P}_{r0})\right]. \tag{20}$$

The equations and implementation, by themselves, make no assumptions about the frequency dependence of κ. Ideally, the correct approach would be to resolve the spectrum of the radiation field, using for example a multigroup method (see, e.g. Vaytet et al. 2011), and compute opacities self-consistently. However, this would render the scheme significantly more computationally expensive, and we thus leave it for future extensions. Instead, for the purposes of this work, we shall adopt the approximation that $\kappa_E \approx \kappa_P$ and $\kappa_F \approx \kappa_R$, where κ_R is the Rossseland mean opacity given by

$$\kappa_R^{-1} = \frac{\int_0^\infty dv_0 \kappa_0(v_0)^{-1}\left[\partial B(v_0, T_0)/\partial T_0\right]}{\int_0^\infty dv_0\left[\partial B(v_0, T_0)/\partial T_0\right]}. \tag{21}$$

The former condition is obtained by assuming the radiation has a blackbody spectrum, and the latter yields the correct radiation force in optically thick media. In equation (14) we use $\kappa = \kappa_P$, which would make it consistent with the equation for E_r in steady state. We note that this choice of opacity would not be consistent with the steady state equation for $\boldsymbol{F}_r$. However, it is not possible for equation (14) to be fully consistent with both the moment equations regardless of the choice of grey opacity κ adopted; only a frequency-dependent opacity can permit this.

---

[5]This is sometimes referred to as a hybrid radiation transfer, and we follow this terminology in this paper.

2.2 Solution algorithm

2.2.1 Algorithm summary

To begin with, it is useful to summarize the series of steps followed by VETTAM in each simulation time-step. We refer the reader to specific subsections for details of each step in the algorithm.

(i) Perform the explicit hydrodynamic update (equation 24) with the hydrodynamic solver capabilities in FLASH.

(ii) If point sources of radiation are present in the simulation, compute and add their direct contribution to the energy $(\dot{E}_*)$ and momentum $(\dot{\boldsymbol{p}}_*)$ of the gas (Section 2.2.6).

(iii) Use the gas variables to compute opacities (κ_P, κ_R) and the source function (S) for the transfer equation. Solve the time-independent transfer equation using the hybrid characteristics ray tracer and compute the Eddington Tensor from the solution $\mathbf{T}$ (Section 2.2.5).

(iv) Perform a linearized first-order backwards Euler implicit update for the equations governing E_r and $\boldsymbol{F}_r$ with the temperature obtained from step ii, keeping the hydrodynamic quantities fixed for this update (Section 2.2.4). This update, converged to a relative tolerance of ϵ_R, provides a guess solution for the radiation quantities $E_{r,*}$ and $\boldsymbol{F}_{r,*}$.

(v) Solve the nonlinear equation for a guess for the gas temperature T_* with Newton's method to a relative tolerance of ϵ_N (Section 2.2.4).

(vi) Repeat steps iv & v until the vector of quantities $\boldsymbol{x}_P = \left[E_{r,*}, \boldsymbol{F}_{r,*}, T_*\right]$ converges to a relative tolerance of ϵ_P. Set the time-updated values for these variables to the converged guess.

(vii) Add the explicitly handled radiation source terms $cG_{0,e}$ (equation 32) and $\boldsymbol{G}$ (equation 8) using the converged solution for $\boldsymbol{x}_P$.

(viii) Update the time $t^{n+1} = t^n + \Delta t$, calculating the new time-step according to a modified Courant-Friedrichs-Lewy (CFL) condition using the adiabatic sound speed for RHD.

The modified time-step here is essentially a modification to the standard CFL condition (Courant, Friedrichs & Lewy 1928), modified to account for the effect of radiation pressure on the propagation of acoustic waves (Mihalas & Mihalas 1984). Following Krumholz et al. (2007a), we use an approximate expression for the effective sound speed,

$$c_{\rm eff} = \sqrt{\frac{\gamma P + (4/9)E_r(1 - e^{-\rho\kappa_R \Delta x})}{\rho}}, \tag{22}$$

where γ is the adiabatic index of the gas, and Δx is the computational cell length on the highest refined level $l_{\max}$, as is the convention in FLASH. The hydrodynamic time-step is then set to

$$\Delta t = C_0 \frac{\Delta x}{\max(|\boldsymbol{v}| + c_{\rm eff})}, \tag{23}$$

where C_0 is the Courant number, and the denominator denotes the maximum signal speed at $l_{\max}$.

2.2.2 Operator-splitting

Equations (1)–(5) are a set of coupled, nonlinear, hyperbolic conservation laws plus source terms, for which various methods exist to obtain solutions. However, the large difference in hydrodynamical sound-crossing and the radiation light-crossing time-scales poses a difficult numerical challenge. In addition, the stiff nonlinear source terms associated with the radiation–gas interaction could render the system sensitive to perturbations and prone to ringing (LeVeque

2002). Thus, we must solve the radiation subsystem, along with the coupled stiff source term update, for the hydrodynamic quantities in an implicit manner. For this purpose, we operator-split this subset of equations from the hyperbolic hydrodynamic update that contains non-stiff source terms, which is treated explicitly using the preexisting infrastructure available in FLASH. We also treat the contribution of radiation source terms in the gas momentum density equation (G in equation 3) explicitly. In the gas energy equation, we treat the update for the stiff gas–radiation interaction term implicitly and by default we treat the other $\mathcal{O}(v/c)$ terms explicitly. However, in some cases where the system is in the dynamic diffusion regime, we found treating these terms implicitly as well rendered the system more robust and stable at larger time-steps, and our software implementation therefore provides a run-time switch to specify whether to treat the non-stiff energy source terms implicitly or explicitly.

Formally, we can express our operator splitting approach in terms of the following sub-problems:

$$\frac{\partial U_e}{\partial t} + \nabla \cdot (\mathbb{F}_e) = S_e, \tag{24}$$

$$\frac{\partial U_r}{\partial t} + \nabla \cdot (\mathbb{F}_r) = S_r, \tag{25}$$

where

$$U_e = \begin{bmatrix} \rho \\ \rho v \\ E \end{bmatrix}, \tag{26}$$

$$\mathbb{F}_e = \begin{bmatrix} \rho v \\ \rho v v + P \mathsf{I} \\ (E + P)v \end{bmatrix}, \tag{27}$$

$$S_e = \begin{bmatrix} 0 \\ -\rho \nabla \Phi + G \\ -\rho v \cdot \nabla \Phi + cG_{0,e} \end{bmatrix}, \tag{28}$$

$$U_r = \begin{bmatrix} E \\ E_R \\ F_r \end{bmatrix}, \tag{29}$$

$$\mathbb{F}_r = \begin{bmatrix} 0 \\ F_r \\ c^2 E_R \mathsf{T} \end{bmatrix}, \tag{30}$$

$$S_r = \begin{bmatrix} -\rho \kappa_P c[a_R T^4 - E_R] \\ -cG^0 \\ -c^2 G \end{bmatrix}. \tag{31}$$

In the expressions above,

$$cG_{0,e} = \rho \left(\kappa_F - 2\kappa_E \right) \frac{v \cdot F_r}{c^2} + \rho \left(\kappa_E - \kappa_F \right) \left[\frac{v^2}{c^2} E_r + \frac{vv}{c^2} : \mathsf{P}_r \right] \tag{32}$$

is the collection of $\mathcal{O}(v/c)$ coupling terms that by default we treat explicitly; in the alternative implicit treatment we move this term from the last element of S_e to the first element of S_r.

We solve subsystem 24 using the pre-existing infrastructure available in FLASH, with the trivial modification of adding the radiation-related source terms G and $cG_{0,e}$ that appear in S_e. We discretize these terms such that E_r and F_r are the values obtained after the implicit update for the radiation quantities, i.e. at time t^{n+1}.

On the other hand, subsystem 25 represents a set of coupled nonlinear equations that we update fully implicitly using a first-order backward Euler differencing in time. We restrict the temporal

accuracy to first-order because higher-order implicit time integration schemes have been found to lead to oscillatory solutions when using large time-steps (Sekora & Stone 2010). We use a Godunov method to discretize the vector flux $\nabla \cdot \mathbb{F}_r$ for the conserved quantities U_r, using an HLLE Riemann solver in an implicit fashion by defining the variables in the flux expression to be at time t^{n+1}. We describe this procedure in further detail in Section 2.2.3. During this stage, we keep the hydrodynamical quantities ρ and v fixed to the state obtained after the hydrodynamic update in the source terms on the right-hand side of equation (25). On the other hand, the radiation quantities E_r and F_r are at time t^{n+1}, as required for an implicit method.

The above discretization approach, when written down for every cell in the domain, leads to a system of nonlinear equations that can be represented in a matrix form, and inverted to obtain a solution. We use a fixed-point Picard iteration scheme to treat the nonlinear update of the implicit subsystem and describe the method in further detail in Section 2.2.4 below. We also note that the Eddington Tensor (**T**), obtained with a solution to the time-independent RT equation, is pre-computed using the physical quantities obtained after the hydrodynamic update, and is kept fixed for the implicit update. In Sections 2.2.5 and 2.2.6, we provide further details on how **T** is obtained with the hybrid characteristics ray-tracing scheme for diffuse sources and for point sources of radiation, respectively.

2.2.3 Implicit hyperbolic transport of radiation

To evolve the hyperbolic transport equations for E_r and F_r in 25, we use a first-order Godunov finite-volume method using a Harten-Lax-van Leer (HLL)-type Riemann solver (Toro 1997) to compute the flux of the conserved variables. With this approach, similar to the one described by Jiang et al. (2012), the discretized evolution equation can be written as

$$\begin{aligned} (U_r)_{i,j,k}^{n+1} =& (U_r)_{i,j,k}^n - \frac{\Delta t}{\Delta x} \left[F_{i+1/2,j,k}^{\text{HLLE}} - F_{i-1/2,j,k}^{\text{HLLE}} \right] \\ &- \frac{\Delta t}{\Delta y} \left[F_{i,j+1/2,k}^{\text{HLLE}} - F_{i,j-1/2,k}^{\text{HLLE}} \right] \\ &- \frac{\Delta t}{\Delta z} \left[F_{i,j,k+1/2}^{\text{HLLE}} - F_{i,j,k-1/2}^{\text{HLLE}} \right] + \Delta t S_r^{n+1}, \end{aligned} \tag{33}$$

where the terms F^{HLLE} are the vector of fluxes for the conserved quantities at each cell interface computed by an HLLE Riemann solver (equation 39 of Sekora & Stone 2010). The left and right states at the interface for the Riemann solver are obtained using a piecewise constant (first-order) reconstruction, using the state of the conserved quantities U_r at time t^{n+1} when computing the HLLE fluxes. The characteristic left/right going wavespeeds ($C_{\text{HLLE}}^{\text{L}}$ and $C_{\text{HLLE}}^{\text{R}}$, respectively) are given by

$$C_{\text{HLLE}} = \sqrt{f} c \sqrt{\frac{1 - e^{-\tau_c}}{\tau_c}}, \tag{34}$$

where

$$\tau_c \equiv (10 \, \Delta \ell \, \rho \, \kappa_R)^2 / (2f), \tag{35}$$

$\Delta \ell$ is the cell thickness and f is the diagonal component of **T** in the direction of the flux. We obtain this relation by using the eigenvalues of the radiation moment equations in the free streaming limit ($\pm \sqrt{f} c$), and applying an optical depth-dependent correction factor following equation A3 of Jiang, Stone & Davis (2013; J13 hereafter) to circumvent the issue of the numerical diffusive flux becoming dominant over the physical diffusion flux in the optically

thick regime (Audit et al. 2002). In Appendix A1, we show that this correction is required to avoid substantial numerical diffusion in simulations where the cell optical depth is $\gg 1$.

However, in our implementation, we introduce a modification to the J13 correction factor for AMR grids. J13 evaluate the correction factor τ_c at a cell interface using the arithmetic mean of the values computed using cell-centred quantities at the left (τ_L) and right (τ_R) cells of the interface. We do the same at all interfaces *except* at AMR level boundaries, where we use the upstream value to avoid biases arising from the different cell sizes on the two sides of the interface. We found this modification to be necessary for obtaining continuous and accurate results with AMR,[6] and justify this choice in Appendix A2. In summary, the value of τ_c at an interface for the right- ($C_{\mathrm{HLLE}}^{\mathrm{R}}$) and left- ($C_{\mathrm{HLLE}}^{\mathrm{L}}$) going waves is

$$\tau_c(\tau_{\mathrm{L}}, \tau_{\mathrm{R}}) = \begin{cases} \frac{\tau_{\mathrm{L}} + \tau_{\mathrm{R}}}{2} & |l_{\mathrm{R}} - l_{\mathrm{L}}| = 0 \\ \tau_L & |l_{\mathrm{R}} - l_{\mathrm{L}}| > 0 \text{ for } C_{\mathrm{HLLE}}^{\mathrm{R}} , \\ \tau_R & |l_{\mathrm{R}} - l_{\mathrm{L}}| > 0 \text{ for } C_{\mathrm{HLLE}}^{\mathrm{L}} \end{cases} \tag{36}$$

where l_{R} and l_{L} are the numbers of the AMR levels of the cells to the right and left of the interface, respectively.

We must also take steps to ensure that the hyperbolic transport of the conserved quantities E_r and F_r retains conservation at cell interfaces where there is a jump in refinement level. For instance, the net transport of radiation energy and momentum out of a coarse cell should be balanced by the corresponding sum of the same entering the finer neighbour cells. However, this condition is not automatically satisfied at AMR level boundaries, since the terms that express the transport fluxes depend on ghost cell data at block boundaries, which are interpolated, and are thus not identical at both sides of the interface. In an explicit method, it is possible to perform a correction step after the hyperbolic update is performed to ensure flux consistency (Berger & Colella 1989). However, this luxury is not available to an implicit method, and flux consistency should either by enforced by construction in the implicit set of equations solved (e.g. Commerçon et al. 2011; Klassen et al. 2014), or through a level-by-level approach with synchronization steps that also allows one to use adaptive time-stepping (e.g. Howell & Greenough 2003; Zhang et al. 2011; Commerçon, Debout & Teyssier 2014). Since FLASH does not include adaptive time-stepping, we chose to adopt the former approach. Specifically, we enforce conservation by replacing the coarse flux determined by the HLLE solver across any coarse-fine interface with the sum of the fine fluxes. For example, consider the case of a 2D coarse-fine interface, and denote the hyperbolic flux out of the coarse cell as $F_{\mathrm{c}}^{\mathrm{HLLE}}$, and that entering the two fine cells to be $F_{\mathrm{f1}}^{\mathrm{HLLE}}$ and $F_{\mathrm{f2}}^{\mathrm{HLLE}}$. Since the fine cells each have face areas equal to half that of the coarse cell, exact conservation requires that

$$F_{\mathrm{c}}^{\mathrm{HLLE}} = \frac{1}{2} \left(F_{\mathrm{f1}}^{\mathrm{HLLE}} + F_{\mathrm{f2}}^{\mathrm{HLLE}} \right) . \tag{37}$$

While in general the HLLE solver will not enforce exact equality, we do in our scheme by explicitly replacing $F_{\mathrm{c}}^{\mathrm{HLLE}}$ with the right-hand side of equation (37) when writing out the discretized equation to be solved. This ensures that our scheme achieves conservation by construction.

2.2.4 *Implicit nonlinear update*

The system of equations described by the subsystem 25 represents a nonlinear coupled set of equations, where the non-linearity arises

due to the stiff gas–radiation interaction term and the nonlinear nature of the temperature dependence of κ_P and κ_R (e.g. Semenov et al. 2003). There exist numerous strategies for solving systems of coupled nonlinear equations (see e.g. Kelley 1995), and our choice is dictated by simplicity and performance. Most commonly, Newton–Raphson iteration methods are used to treat such systems; however, they require the computation of the Jacobian of the system, which in our case is unavailable analytically, and would be expensive to compute numerically. While there exist Jacobian-free Newton–Krylov methods to circumvent costs associated with constructing the Jacobian (Knoll & Keyes 2004), we adopt a simpler, yet robust, fixed-point Picard iteration scheme.[7] Picard iteration is a method for solving a system of nonlinear equations by reformulating them as the problem of finding the fixed point of a function (Kelley 1995; Burden & Faires 1997). This is done by starting with an initial guess for the solution to the nonlinear system, and successively improving the guess through the solution of a simpler linearized recasting of the nonlinear system of equations.

We implement the Picard iteration method in our scheme in the following fashion: we first operator-split the gas energy update from the radiation moment equations, and then discretize the term proportional to T^4 in the latter to use a provided guess temperature T_*, which we set to the old time value (T_n) at the start of the update. The first-order Euler backward update for a time-step $\Delta t = t_{n+1} - t_n$ can be written for each computational cell as

$$\frac{E_{r,*} - E_{r,n}}{\Delta t} + \nabla \cdot \boldsymbol{F}_{r,*} = cG_*^0 \tag{38}$$

$$\frac{\boldsymbol{F}_{r,*} - \boldsymbol{F}_{r,n}}{\Delta t} + c^2 \nabla \cdot \mathbf{T} E_{r,*} = c\boldsymbol{G}_* , \tag{39}$$

where the source terms cG_*^0 and $\boldsymbol{G}_*$ use the guess temperature T_*, and corresponding opacities $\kappa_P(T_*)$, $\kappa_R(T_*)$ in their expressions. The discretization described here effectively linearizes the implicit radiation moment equation update, and we use sparse matrix solvers based on Krylov subspace methods (Saad 2003) offered by the PETSc library to obtain the solution to $E_{r,*}$ and $\boldsymbol{F}_{r,*}$. We use the generalized minimum residual (GMRES) solver (Saad & Schultz 1986) by default, but allow users to choose other solvers and pre-conditioners at run time. We use the default convergence criteria in PETSc based on the 2-norm of the preconditioned residual to check for convergence to a user-defined relative tolerance ϵ_{R}. The guess for the gas temperature is then improved by implicitly updating the gas energy as

$$\frac{E_* - E_n}{\Delta t} = -\rho \kappa_P c \left[a_R T_*^4 - E_{r,*} \right] , \tag{40}$$

where κ_P is identical to that used in equations (38) and (39), and $E_* - E_n = \alpha(T_* - T_n)$, using the relation between internal energy and temperature $E_{\mathrm{int}} = \alpha T$, and the fact that the discretization we use ensures the kinetic energies cancel out. This represents a nonlinear equation for the new temperature guess T_*, which is, however, local, and hence we can solve this independently for each cell. We use a simple Newton's method by analytically constructing the Jacobian of the polynomial equation (40) to obtain T_*, assessing convergence on the relative tolerance of the temperature ϵ_{N}. The combination of the implicit radiation subsystem update, and the implicit gas temperature update comprise *one* Picard iteration. At the end of each iteration,

---

[6]The implementation of J13 was for uniform grids, and hence did not face the aforementioned issue.

[7]This iterative method is also sometimes called nonlinear Richardson iteration, or the method of successive substitution.

we check for the residual change in the vector

$$\boldsymbol{x}_{\mathrm{P}} = \begin{bmatrix} E_r \\ \boldsymbol{F}_r \\ T \end{bmatrix}, \tag{41}$$

over the iteration, and check for convergence within a relative tolerance ϵ_{P}. If convergence is satisfied, we set the new time solution for E_r, $\boldsymbol{F}_r$, and T to be equal to the guess in the last Picard iteration, and if not we repeat the procedure, using the values obtained at the end of this iteration as our new guess.

One may notice that the radiation–gas interaction terms in equations (38) and (40) are not the same by construction, with the former using a guess temperature T_* in cG_*^0 that is lagged by one Picard iteration as compared to the T_* used in the latter. This, in some cases, can lead to non-conservation of total energy in the domain. We thus add a correction term ΔE explicitly in each Picard iteration to the right-hand side of equation (40) accounting for this variation in discretization. This has the form

$$\Delta E = \rho \kappa_P c a_R \left[T_{n,*}^4 - T_{o,*}^4 \right], \tag{42}$$

where $T_{o,*}$ is the value of T_* used in the last update of equation (38), and $T_{n,*}$ is that used in the last update of equation (40). This ensures that energy is conserved irrespective of the adopted value of ϵ_{P}. However, we note that since we use implicit updates for equations (38) and (40), we cannot ensure strict convergence of energy to machine precision, and are limited to the precision ϵ_{N} and ϵ_{R}.

2.2.5 Computing the Eddington tensor

The VET, used to close the radiation momentum equations with equation (13), is calculated explicitly from a formal solution of the time-independent RT equation (equation (14)). We use a hybrid-characteristics based raytracing approach to solve this equation on large sets of characteristics (rays) using the implementation in FLASH by Buntemeyer et al. (2016). We use the obtained solution for the grey radiation intensity (I_r) from the ray tracer, perform angular quadratures on it to compute E_r and $\mathbf{P}_r$, and use them to obtain $\mathbf{T}$ using equation (13). To avoid having to allocate and store the specific intensity over all angles and spatial locations, we compute the quadratures on-the-fly for the intensity along each ray in space. The discretized quadrature contributions are given by

$$E_r = \frac{c}{4\pi} \sum_{k=0}^{N_\Omega - 1} w_k I_{r,k}, \tag{43}$$

and

$$\mathbf{P}_r = \frac{c}{4\pi} \sum_{k=0}^{N_\Omega - 1} w_k I_{r,k} \mu_{ik} \mu_{jk}, \tag{44}$$

where $I_{r,k}$ is the intensity along a ray in the direction $\hat{\boldsymbol{n}}_k$, w_k is the quadrature weight, $\mu_{ik} = \hat{\boldsymbol{n}}_k \cdot \hat{\boldsymbol{x}}_i$, where $\hat{\boldsymbol{x}}_i$ is the unit vector along the coordinate axis i, and the quadrature sum is performed over N_Ω discrete angles. We use the HEALPIX tesselation scheme to discretize angles on the unit sphere uniformly, which allows values of $N_\Omega = 12 N_{\mathrm{side}}^2$, where N_{side} is an integer that is a power of 2 (i.e. $N_{\mathrm{side}} = 1, 2, 4, 8,...$). We expect the appropriate value of N_Ω to use to be problem-dependent; however, we find reasonable results for our tests even with moderate N_Ω, as shown in Appendix B. We also randomly rotate the angles generated by the HEALPIX tesselation to prevent accumulation of artefacts introduced by the discretization (see e.g. Krumholz, Stone & Gardiner 2007b). We note that the VET

is computed at the start of the time-step, and kept fixed for the overall radiation system update described in Section 2.2.4.

2.2.6 Point sources contribution

VETTAM is a hybrid radiation transport scheme, i.e. it splits the radiation field into a direct and diffuse component (Wolfire & Cassinelli 1986; Murray et al. 1994), where the direct component includes the contributions from point sources implemented with sink particles (Federrath et al. 2010), and the diffuse component involves the diffuse (re-)emission of (thermal) radiation by the dust. The latter is handled by the radiation moment equations closed with the VET described above. The direct contribution is handled solely by the hybrid-characteristics ray tracer, which solves equation (14) along rays that originate at point sources in the domain, with no effective emission, i.e. $S = 0$. This splitting is useful if a simulation includes sink particles to represent stars or clusters, whose contribution to the radiation field can be quite asymmetric depending on the matter distribution. This splitting approach also allows a frequency-dependent treatment of the direct radiation (e.g. Kuiper et al. 2010; Rosen et al. 2016), which often has a very different colour temperature than the reprocessed radiation, and thus experiences very different matter opacities (see Kuiper et al. 2012, for a direct comparison). The ray trace is performed using the implementation originally described in Rijkhorst et al. (2006), and improved later by Peters et al. (2010) and Buntemeyer et al. (2016). The ray tracer computes effective optical depths from a point source to each cell in the domain and used to obtain the energy ($\dot{E}_*$) and momentum ($\dot{\boldsymbol{p}}_*$) deposited in the gas. The energy deposition rate $\dot{E}_*$ absorbed by the gas in a computational cell at a distance r from the star is given by

$$\dot{E}_* = \frac{L_* e^{-\tau_*} \left(1 - e^{-\tau_{\mathrm{cell}}} \right)}{4\pi r^2 \Delta r}, \tag{45}$$

where L_* is the luminosity of the point source, τ_* is the optical depth to the cell for a ray originating at the point source, $\tau_{\mathrm{cell}} = \rho \kappa_* \Delta r$ is the local optical depth of the cell, where κ_* is the opacity to the direct radiation, and Δr is the length of the ray intersected by the cell. For numerical stability, when τ_{cell} is very small, $\dot{E}_*$ is estimated by a Taylor-expanded form of the above relation given by

$$\dot{E}_* = \frac{\tau_{\mathrm{cell}} L_* e^{-\tau_*}}{4\pi r^2 \Delta r}. \tag{46}$$

The momentum contribution rate $\dot{\boldsymbol{p}}_*$ is given by

$$\dot{\boldsymbol{p}}_* = \frac{\dot{E}_*}{c} \hat{\boldsymbol{r}}, \tag{47}$$

where $\hat{\boldsymbol{r}}$ denotes the direction of the ray to the cell from the point source.

3 NUMERICAL TESTS

In this section, we provide numerical tests of the scheme described in the previous sections. We compare our numerical results (f_{num}) with analytic or semi-analytic solutions (f_{an}) when available, using either the L_1 relative norm or the maximum relative error L_{max} defined by

$$L_1 = \frac{\sum_i |f_{\mathrm{num,i}} - f_{\mathrm{an,i}}| \, \Delta x_i}{\sum_i f_{\mathrm{an,i}} \Delta x_i}, \tag{48}$$

and

$$L_{\mathrm{max}} = \max_i \left[\frac{|f_{\mathrm{num,i}} - f_{\mathrm{an,i}}|}{f_{\mathrm{an,i}}} \right], \tag{49}$$

where i can denote the solution at a spatial location or time t_i for the problem. We use the following settings for our tests, unless otherwise specified: relative tolerances of $\epsilon_N = \epsilon_R = 10^{-6}$ and $\epsilon_P = 10^{-3}$, GMRES solver left-preconditioned with the additive Schwarz method for the implicit radiation update, and a Courant number $C_0 = 0.8$. We also do not use gravity in any of our tests (i.e. $\phi = 0$).

3.1 Radiating pulse

In our first test, we evolve the propagation of a 1D Gaussian pulse of radiation energy in a static medium ($v = 0$), for three different opacities (κ_0), that correspond to the streaming ($\tau \ll 1$), weak equilibrium diffusion ($\tau \sim 1$), and strong equilibrium diffusion ($\tau \gg 1$) regimes, respectively. In the streaming regime, radiation and hydrodynamics are decoupled and the resulting dynamics resemble an advection process. In the diffusion limits, radiation and hydrodynamics are strongly coupled, and the resulting dynamics resemble a diffusion process. We perform this test to demonstrate that our scheme is capable of reproducing the right solutions in all regimes of radiation transport. The test setup is a 1D domain ranging from $x = -x_0$ to $x = x_0$, where $x_0 = 0.5$ cm for the streaming test, and $x_0 = 5$ cm for the diffusion tests, respectively; the domain size is larger in the diffusion tests so that we can capture the diffusion of the pulse for longer times without boundary effects coming into play. The density of the gas for all cases is fixed to $\rho = 10^{-20}$ g cm^{-3}, and we disable hydrodynamics, so ρ does not evolve and the gas velocity remains $v = 0$. The initial radiation energy density is

$$E_r(x, 0) = E_0 \exp\left(-\mu^2 x^2\right), \tag{50}$$

where we set $E_0 = 1$ erg cm^{-3} and $\mu = 20$ cm^{-1}. Since the purpose of this test is to check whether our scheme captures the physical transport/diffusive fluxes accurately, we set $\kappa_E = 0$ and $\kappa_F = \kappa_0 = 1, 4 \times 10^{21}$, and 4×10^{24} cm^2 g^{-1} for the streaming, static diffusion, and equilibrium diffusion versions, respectively; this has the effect of disabling energy exchange between gas and radiation (since all exchange terms are proportional to either κ_E or v, both of which are zero), and thus mimics the effects of a purely scattering medium. For the streaming test, we initialize the radiation flux to the streaming solution,

$$F_r(x, 0) = c E_r(x, 0), \tag{51}$$

whereas we use the solution expected for pure diffusion for diffusion tests, i.e.

$$F_r(x, 0) = \frac{-c}{3\rho\kappa_0} \frac{\partial E_r(x, 0)}{\partial x} = \frac{2c\mu^2 x^2}{3} E_r(x, 0). \tag{52}$$

We do not use the ray tracer for this test as the Eddington tensor component (f_{xx}) is spatially and temporally uniform with a value of $f_{xx} = 1$ for the streaming test and $f_{xx} = 1/3$ for the others. We evolve the system at the light crossing time-scale across a cell, i.e. $\Delta t = \Delta x/c$, where Δx is the cell thickness. We use a resolution of 1024 cells for our tests and adopt periodic (outflow) boundary conditions for the streaming (diffusion) tests. In the streaming limit, the exact solution is a radiation energy density profile identical to the initial state, displaced by ct in the direction of the initial flux, i.e.

$$E_r(x, t) = E_r(x - ct, 0). \tag{53}$$

In the diffusion tests, one can obtain an analytic solution by the method of Green's functions, which gives

$$E_r(x, t) = \frac{1}{\left(4Dt\mu^2 + 1\right)^{1/2}} \exp\left(\frac{-\mu^2 x^2}{4Dt\mu^2 + 1}\right). \tag{54}$$

The corresponding flux is $F_r(x, t) = -D(\partial E_r(x, t)/\partial x)$, where $D = c/3\kappa_0\rho$ is the diffusion coefficient.

We compare the exact and numerical results we obtain for the radiation energy (E_r) for three times in all three cases in Fig. 1. We see that the agreement with the analytical solutions is good, especially for the diffusing pulses. The L_1 relative errors for the three time instances shown in Fig. 1 for the static diffusion test are 5 per cent, 3.7 per cent, and 3.3 per cent, and for the equilibrium diffusion test are 2.4 per cent, 3 per cent, and 3.2 per cent. The agreement is poorer for the streaming pulse though, especially at later times, with L_1 relative errors of 3.7 per cent, 16 per cent, and 27 per cent, respectively. Although we capture the propagation speed (hence, position) of the pulse accurately in the streaming regime, we find that the pulse has diffused from its initial true state due to numerical diffusion at later times. This is not surprising considering that our scheme is only first-order accurate in space and time. In addition, it is widely known that implicit methods perform poorly when trying to capture the propagation of individual wave modes (Sekora & Stone 2010). We keep these limitations in mind, and aim to address this with higher-order reconstruction strategies in future versions of the code.

3.2 Dynamic diffusion test

The dynamic diffusion regime ($\tau\beta \gg 1$) is a regime of high optical depth where the photons are effectively trapped in the fluid so strongly that radiation transport is primarily by the advection of photons by the gas, rather than diffusion of photons through the gas. Reproducing this limit of RHDs requires accurate handling of the $\mathcal{O}(v/c)$ source terms in the radiation moment equations. To test whether our scheme can achieve this, we setup a Gaussian pulse test with a domain and initial conditions similar to those used in diffusion tests in the previous section, including the condition of $\kappa_E = 0$. However, we increase the value of $\kappa_F = \kappa_0 = 4 \times 10^{26}$ cm^2 g^{-1}, and initialize the gas with a velocity $v = 3$ km s^{-1} in the positive x direction rather than 0. The Eddington approximation is used to estimate the Eddington tensor. In addition, we also take care to modify the initial values of E_r and F_r, which are defined in the lab frame in our scheme, by performing the appropriate Lorentz transformation from the comoving frame initial conditions [given by equations (50) and (52)] to the lab frame (Mihalas & Mihalas 1984). The domain is discretized with 2048 uniformly spaced cells.

We show our numerical results in Fig. 2 for times corresponding to 25 per cent, 50 per cent, and 100 per cent of the domain crossing time. We compare this solution with the expected analytical solution for this system, which in the comoving frame should be identical to equation (54). In the simulation frame, the corresponding solution is

$$E_r(x, t) = \frac{1}{\left(4Dt\mu^2 + 1\right)^{1/2}} \exp\left(\frac{-(\mu(x - vt))^2}{4Dt\mu^2 + 1}\right). \tag{55}$$

We find that our numerical solution is in good agreement with the analytical one, with L_1 relative errors of 4.5 per cent, 5.6 per cent, and 5.8 per cent, respectively for the three timestamps shown in Fig. 2. This test demonstrates the capability of our scheme to perform correctly in the dynamic diffusion regime.

3.3 Non-equilibrium radiation-matter coupling test

In this problem, we test our treatment of the gas-radiation coupling term as implemented with a fixed-point Picard iteration scheme described in Section 2.2.4. We setup the problem in a fashion similar
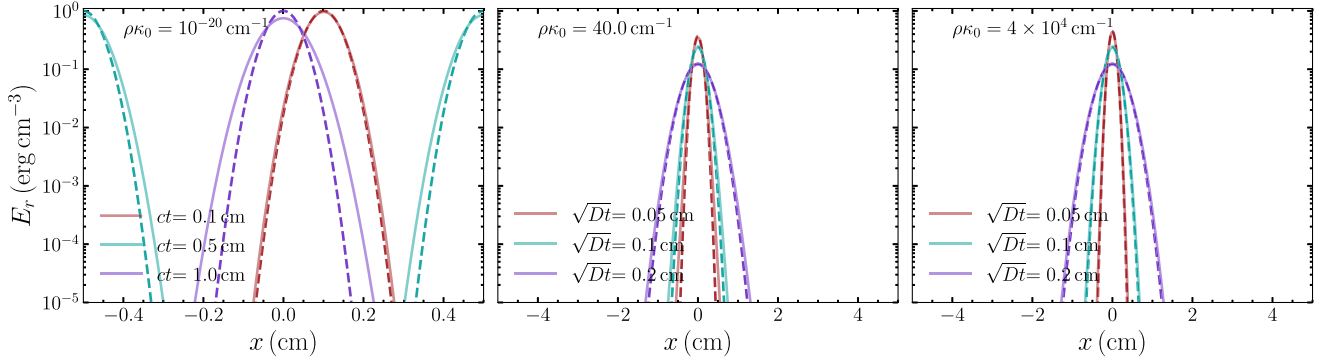
Figure 1. Radiation pulse in the streaming (left), weak equilibrium diffusion (middle), and strong equilibrium diffusion (right) regimes for three different times, with their corresponding analytical solutions given by equation (53; streaming) and equation (54; weak/strong diffusion) overplotted (dashed lines). We indicate the total opacity ($\rho\kappa_0$) for each version in the top-left corner of the plot.
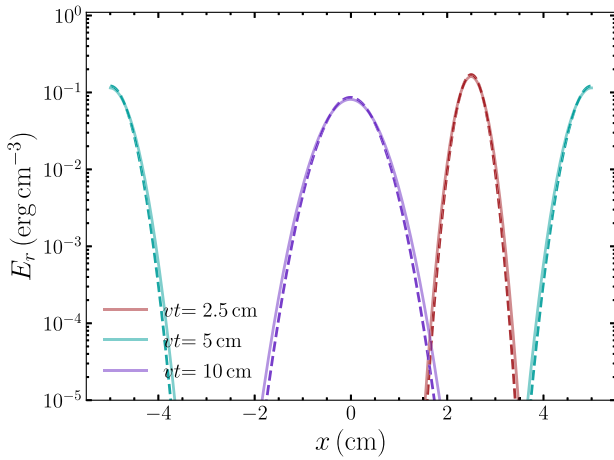

Figure 2. Lab-frame radiation energy density (E_r) for a Gaussian radiation pulse in the dynamic diffusion regime, with $\rho\kappa_0 = 4 \times 10^6$ cm^{-1} and $v/c \sim 10^{-5}$, for three different times corresponding to 25 per cent, 50 per cent, and 100 per cent of the domain crossing time. Solid lines show the numerical solution we obtain, while dashed lines indicate the corresponding analytical solutions.

Figure 3. Evolution of the gas (T_g; circles) and radiation temperatures (T_r; squares) for the gas-radiation coupling test described in Section 3.3 as a function of time (t) scaled by the thermalization time-scale $t_{\text{therm}} = 3.33 \times 10^{-11}$ s. We perform the test for values of $\mathbb{P} = a_R T_{g,0}^4/(\rho R T_{g,0})$ of 10^{-9} (red), 10 (cyan), and 10^{11} (violet), denoting varying levels of gas thermal inertia. We overplot, with solid lines, the final thermal equilibrium state T_{eq} for each case, obtained from the solution to the fourth-order polynomial equation (56).

to Jiang (2021), with an initial state where the gas and radiation temperatures are out of equilibrium ($|a_R T^4 - E_r| \geq 0$), to test whether the temperatures approach the correct state corresponding to thermal equilibrium ($a_R T^4 = E_r$). A uniform box is initialized in the region [0,1] cm, discretized with 512 cells, with a fixed specific opacity $\rho\kappa_P = 1$ cm^{-1} and an ideal gas $\gamma = 5/3$. The gas temperature is $T = T_{g,0} = 100$ K everywhere, and the radiation energy $E_{r,0} = 7.567 \times 10^{-13}$ erg cm^{-3}, which leads to a radiation temperature $T_{r,0} = (E_{r,0}/a_R)^{1/4} \approx 3.16$ K. The boundary conditions are set to be zero-gradient outflow boundaries in E_r and F_r. We test the setup with three different values of $\rho = 10^{-7}$, 10^{-17}, and 10^{-27} g cm^{-3}, respectively. We parametrize these three setups in terms of the dimensionless ratio $\mathbb{P} = a_R T_{g,0}^4/(\rho R T_{g,0})$ where R is the ideal gas constant; our three cases correspond to values of $\mathbb{P}_0 = 10^{-9}$, 10, and 10^{11}, respectively. The three versions represent varying levels of thermal inertia of the gas, with a lower (higher) value of $\mathbb{P}_0$ indicating a higher (lower) gas thermal inertia, which means that the radiation (gas) temperature changes more significantly to reach the final equilibrium state. The tests are run up to a final time of $t = 5t_{\text{therm}}$, where $t_{\text{therm}} = 1/(\rho\kappa_P c) = 3.33 \times 10^{-11}$ s is the
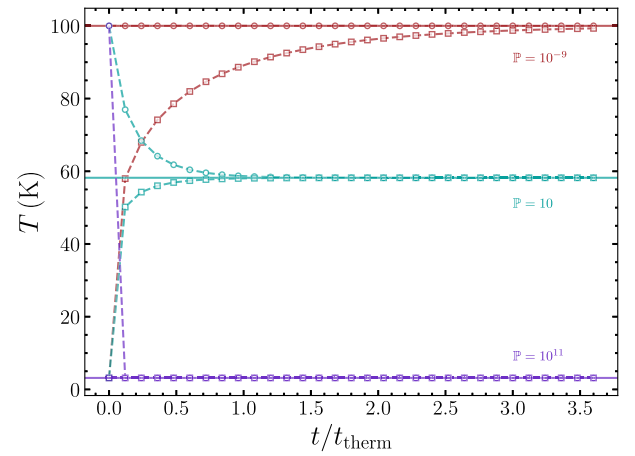
typical thermalization time-scale. We show the time evolution of T and T_r for the three cases in Fig. 3. We can compare the final thermal equilibrium state we obtain $T_{g,\text{eq}} = T_{r,\text{eq}} = T_{\text{eq}}$ with that obtained analytically by enforcing total (gas+radiation) energy conservation in the initial and equilibrium states, i.e.

$$\frac{\rho R T_{g,0}}{\mu(\gamma - 1)} + a_R(T_{r,0})^4 = \frac{\rho R T_{\text{eq}}}{\mu m_H(\gamma - 1)} + a_R(T_{\text{eq}})^4, \quad (56)$$

where $\mu = 0.6 m_H$ is the mean particle mass of the gas, and m_H the mass of the hydrogen atom. The fourth-order polynomial equation above can be solved to obtain T_{eq}, and we also show this solution in Fig. 3. We find that the final state obtained in our numerical solution agrees with the analytically obtained value of T_{eq} to within 10^{-8} in all cases. In addition, we also verify that the total energy in our scheme is conserved to the precision of the implicit radiation update tolerance and/or the nonlinear Newton–Raphson update tolerance (whichever is higher). Overall, the results of this test demonstrate

that the Picard iteration scheme described in Section 2.2.4 captures the nonlinear gas-radiation coupling accurately.

3.4 Non-equilibrium Marshak wave

The Marshak wave is a standard 1D non-equilibrium diffusion test originally proposed by Marshak (1958), for which a semi-analytic solution has been provided by Su & Olson (1996). The domain is initially setup as a cold uniform medium ($T = 0$) with a constant absorption opacity $\sigma = \rho\kappa_P$, and at $t = 0$ a constant radiation flux $F_r^{\rm inc}$ is applied at the $x = 0$ boundary. The propagation of the radiation front heats the gas, and the time evolution is governed by the nonlinear equations of radiation diffusion and radiation-gas energy exchange. This is not a dynamical test, so the hydrodynamic evolution is switched off, with the exception of the thermal energy evolution due to radiation-gas energy exchange as described in Section 2.2.4. In addition, following Su & Olson (1996), we simplify the problem originally proposed by Marshak (1958), in two ways. First, we adopt the Eddington approximation ($f_{\rm xx} = 1/3$). Second, we adopt a specific heat capacity at constant volume for the fluid $C_v = \partial E_{\rm int}/\partial T = \alpha T^3$, where $E_{\rm int}$ is the gas internal energy and α is a fixed constant. The combination of these conditions allows a similarity transformation that converts the partial differential equations for the evolution of E_r and T into a system of Ordinary Differential Equations (ODE's), for which Su & Olson (1996) provide a solution in terms of the dimensionless position $\chi = \sigma x$, and time $\tilde{t} = \epsilon c\sigma t$, where $\epsilon = 4a_R/\alpha$ is a fixed parameter. This solution is expressed in terms of the dimensionless radiation energy density $\mathcal{U}(\chi, \tau) = cE_r(x, t)/(4F_r^{\rm inc})$ and gas temperature $\mathcal{V}(\chi, \tau) = ca_R T^4(x, t)/(4F_r^{\rm inc})$.

We simulate the problem on a 1D grid of resolution $N_x = 1024$, on the domain $x \in [0, 0.5]$ cm, with a uniform background density $\rho = 10^{-20}$ g cm^{-3}, and opacities $\kappa_P = \kappa_R = 4 \times 10^{21}$ cm^2 g^{-1}, leading to a value of $\sigma = 40$ cm^{-1}. The gas and radiation temperature are initialized to zero, and we use a value of $\epsilon = 4a_R/\alpha = 0.1$. The condition of a constant, half-isotropic incoming flux at the $x = 0$ boundary is imposed through the so-called Marshak boundary condition, given by the constraint

$$cE_r(0, t) + 2F(0, t) = 4F_{\rm inc} \tag{57}$$

where $E_r(0, t)$ and $F(0, t)$ are the values of the radiation energy and flux at the boundary wall/interface. We setup the boundary to mimic a source of radiation temperature $k_B T_{\rm inc} = 4.68 \times 10^{-13}$ eV, corresponding to $F_{\rm inc} = a_R c T_{\rm inc}^4/4 = 7.49 \times 10^{49}$ erg cm^{-2} s^{-1}. The other boundary ($x = 0.5$) is set to be reflective, though this choice does not matter since we halt the test before the advancing Marshak wave reaches it. We evolve the system at the light crossing time-scale across a cell, up to a time corresponding to $\tilde{t} = 100$, corresponding to a physical time $t = 8.33 \times 10^{-10}$ s.

We plot our simulation results for $E_r(x, t)$ and $a_R T(x, t)^4$ at $\tilde{t} = [0.1, 1, 10, 100]$ in Fig. 4. We compare this to the Su & Olson (1996) solution for the dimensionless quantities $\mathcal{U}(\chi, \tau)$ and $\mathcal{V}(\chi, \tau)$, which we compute using a publicly available code[8] to numerically integrate their semi-analytic expressions with the parameters of our problem setup. We then rewrite these dimensionless quantities in terms of their dimensional counterparts. We find that our numerical solution reproduces the analytical quite accurately, especially at later times. At earlier times, the agreement is poor, as expected for a scheme that solves the full hyperbolic two-moment system of equations (see González et al. 2007; Skinner & Ostriker 2013; Tsang

---

& Milosavljević 2015, for other two-moment schemes that report similar disagreements), since the Su & Olson (1996) solution uses the diffusion approximation, which is inaccurate at early times when the wave has traversed an optical depth $\ll 1$; the error is that the diffusion approximation allows an infinite signal speed, while our two-moment scheme correctly captures the finite speed of light. This explains why our solution at early times lags the Su & Olson (1996) solution; however, at these times our numerical solution is almost certainly more accurate. In any event, the very good agreement we obtain at late times, when Su & Olson's diffusion approximation is accurate, shows that our scheme correctly reproduces the diffusion limit.

3.5 Non-equilibrium radiation shock

The non-equilibrium radiation shock problem is a test of the non-equilibrium, fully coupled, RHDs system in the presence of shocks in an optically thick medium. This problem has been discussed in classical tests of RHDs (Zel'dovich & Raizer 1967; Mihalas & Mihalas 1984), with analytical solutions available under some physical conditions, namely cases where the material energy dominates the radiation energy, and/or under equilibrium conditions. More recently, however, Lowrie & Edwards (2008) consider the non-equilibrium, high radiation energy density regime – where radiation momentum/energy contributions are significant – and provide a semi-analytic procedure to compute solutions for them. They show that the shock structure is fully determined by five parameters: (i) the dimensionless pressure ratio $\mathbb{P}_0 = a_R T^4/(\rho a^2)$ where T, ρ, and a are the temperature, gas density, and adiabatic sound speed in the upstream regions, (ii) the dimensionless specific opacity $\sigma_0 = \sigma_a Lc/a$, where $\sigma_a \equiv \sigma_a(\rho, T)$ is the absorption-specific opacity, and L is the reference length scale, (iii) the dimensionless diffusion coefficient $D_0 = c/(3\sigma_t La)$ where $\sigma_t \equiv \sigma_t(\rho, T)$ is the total specific opacity, (iv) the adiabatic index γ, and (v) the upstream Mach number $\mathcal{M}_0 = v/a$, where v is the velocity of the shock in the upstream region.

In our test, we use the parameters $\gamma = 5/3$, a spatially uniform $\sigma_0 = 10^6$, $D_0 = 1$, $\mathbb{P}_0 = 10^{-4}$, and $\mathcal{M}_0 = 3$ for the upstream state, from which we derive the corresponding physical conditions in cgs units, in which our code works. This set of parameters corresponds to a subcritical shock in which the pre-shock matter is preheated by the radiation to a temperature lower than the temperature in the downstream relaxation region. We initialize the problem in a domain $x \in [-0.0132, 0.00255]$ cm, with the shock initially placed at $x = 0$. The upstream state of the gas ($x < 0$) is set to be $\rho = 5.69$ g cm^{-3}, $T = 2.18 \times 10^6$ K, and $v = 5.19 \times 10^7$ cm s^{-1}, and, by using the Rankine–Hugoniot jump conditions [by solving equations 12 and 13 of Lowrie & Rauenzahn (2007)], we obtain the downstream state $\rho = 17.1$ g cm^{-3}, $T = 7.98 \times 10^6$ K, and $v = 1.73 \times 10^7$ cm s^{-1}. The absorption-specific opacity is fixed at $\rho\kappa_P = \rho\kappa_R = 577$ cm^{-1} everywhere in the domain, enforced by setting $\kappa_P = \kappa_R = 577/\rho$ cm^2 g^{-1}. This condition on the opacity, although unphysical, is enforced to mimic the solutions provided in Lowrie & Edwards (2008). The gas and radiation are initialized to be in equilibrium at $t = 0$, and we use an ideal monoatomic gas EOS ($\gamma = 5/3$) with a mean particle mass $\mu = m_{\rm H}$. We evolve the system to a time $t = 10^{-9}$ s, corresponding to about three crossing times of the computational domain. The boundary conditions at the lower (higher) x boundary is fixed to the asymptotic downstream (upstream) state of the shock provided in the initial conditions. We also use the Eddington approximation ($f_{\rm xx} = 1/3$) for this problem to allow comparison with the semi-analytical solution derived under the

---

[8] http://cococubed.asu.edu/research_pages/su_olson.shtml
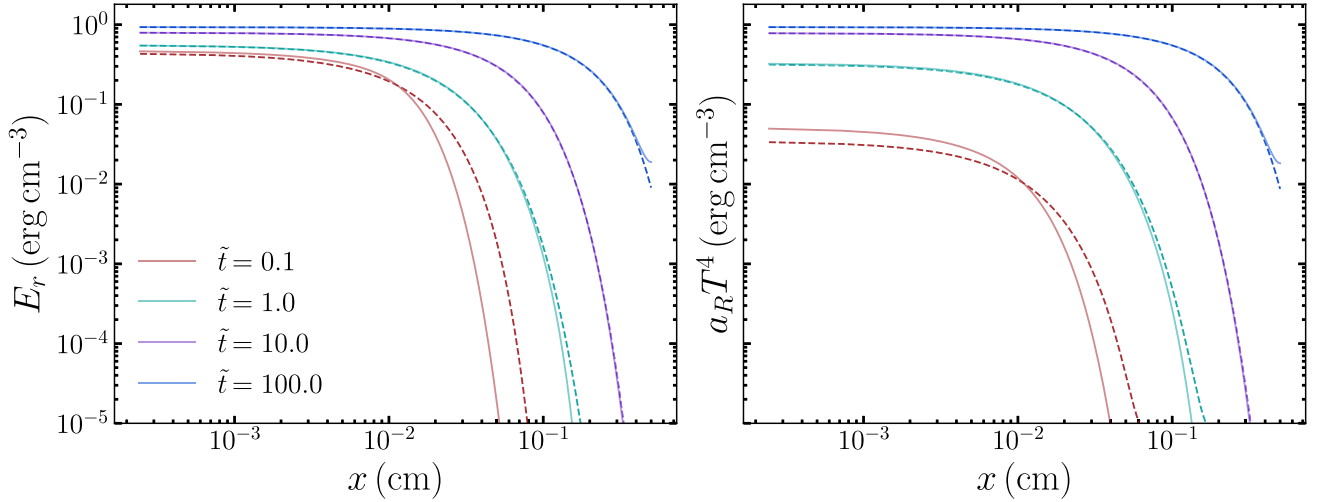
Figure 4. Results for the non-equilibrium Marshak wave test described in Section 3.4. Solid lines indicate the simulation results for E_r (left) and $a_R T^4$ (right) for dimensionless times $\tilde{t} = 0.1, 1, 10,$ and 100. Dashed lines indicate the corresponding solutions at these times obtained by numerically integrating the semi-analytic expressions of Su & Olson (1996).
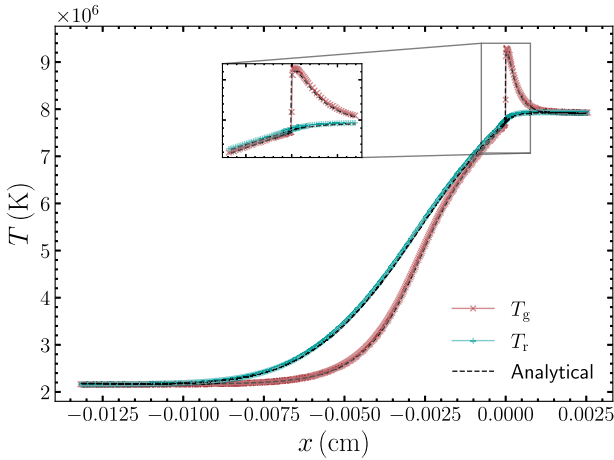

Figure 5. Gas (T_g; red crosses) and radiation (T_r; green plus signs) temperatures for a subcritical non-equilibrium radiative shock; the inset shows the Zel'Dovich spike in detail. The semi-analytical solution of Lowrie & Edwards (2008) is overplotted with black dashed lines.

same assumption. The grid is discretized with a base grid resolution of 640 cells, and adaptively refined on the gas temperature, using the default refinement condition in FLASH based on a modified second derivative of a variable (Fryxell et al. 2000), to a maximum refinement level of $l_{max} = 3$, corresponding to a maximum resolution of 2560 cells. We use the modified CFL time-step criterion (equation (23)) for this problem, with a CFL number $C_0 = 0.5$.

In Fig. 5, we plot the numerical solution we obtain for the gas (T_g) and radiation (T_r) temperatures, with the inset showing the so-called Zel'Dovich spike – an inherently non-equilibrium feature – in further detail. We overplot the solution obtained with the Lowrie & Edwards (2008) semi-analytical procedure as well for comparison. We find very good agreement between the two solutions, with a relative error in the L_1 norm of ~ 0.6 per cent in T and T_r, and find that the sharp temperature spike is well-captured by our refined domain. This test demonstrates that our scheme is able to accurately

capture fully coupled radiation-gas dynamics in the presence of strong discontinuities.

3.6 Advecting radiation pulse

To test the accuracy of our implementation of the $\mathcal{O}(\beta\tau)$ relativistic correction source terms that arise from the mixed frame formulation of the RHD moment equations, in a fully-coupled RHD problem, we simulate the test described by Krumholz et al. (2007a). The test involves the advection of a pulse of radiation energy in an optically thick gas, with a uniform background flow velocity. The initial condition is such that the system is in both pressure and radiative equilibrium everywhere, but with a Gaussian-shaped pulse centred at $x = 0$ within which there is a local increase in the temperature and radiation pressure, and a corresponding decrease in the gas pressure and density. At times $t > 0$, radiation diffuses out of the pulse, leading to the loss of pressure balance, and the gas starts to move into the region occupied by the pulse. While a time-dependent solution is not known analytically, the problem is none the less a useful test if we perform two cases of the setup: one where the gas is initially at rest ($v = 0$), and another where the gas is provided an initial uniform velocity ($v = v_0$). If the velocity-dependent terms are included correctly, the solutions for the two cases should be identical to each other except for displacement by a distance $v_0 t$.

To setup this problem, we initialize the temperature as a function of position to

$$\frac{T}{T_0} = 1 + \exp\left(-\frac{x^2}{2w^2}\right), \tag{58}$$

where $w = 24$ cm is the pulse width and $T_0 = 10^7$ K is the background temperature. Imposing the conditions of radiative and pressure equilibrium everywhere immediately gives the corresponding gas density,

$$\rho = \rho_0 \frac{T_0}{T} + \frac{a_R \mu}{3 k_B}\left(\frac{T_0^4}{T} - T^3\right), \tag{59}$$

where $\rho_0 = 1.2$ g cm^{-3} is the background gas density, and $\mu = 2.33 m_H$ is the mean particle mass. We use a spatially uniform

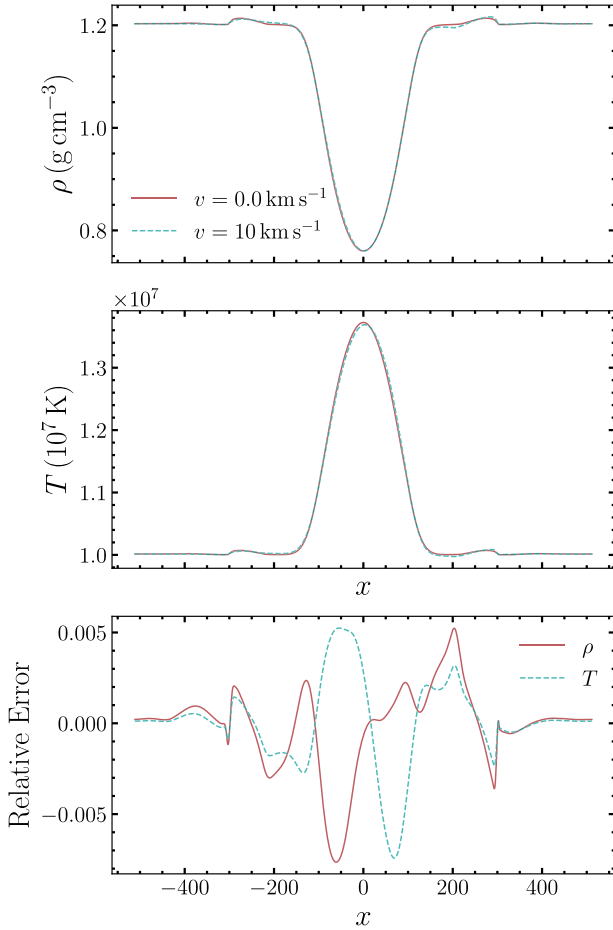**Figure 6.** Plot comparing the density ρ (top) and the gas/radiation temperature T (middle panel) profiles we obtain with our scheme for an initially unadvected (red) and advected (cyan) gas with the radiating pulse advection test of Krumholz et al. (2007a). The bottom panel shows the relative error between the two cases for ρ (red) and T (cyan), which we find to be bounded by 0.7 per cent over the domain.

grey opacity of $\kappa_P = \kappa_R = \kappa_0 = 100\,\mathrm{cm^2\,g^{-1}}$, and use a value of $v_0 = 10\,\mathrm{km\,s^{-1}}$ for the moving pulse case. The simulation domain goes from -512 to $512\,\mathrm{cm}$ and is resolved by 1024 uniformly spaced cells. The Eddington tensor is assumed to be spatially and temporally uniform with a value $f_{xx} = 1/3$. Periodic boundary conditions are used on the radiation and gas, and the system is evolved to a final time of $t = 2w/v_0 = 4.8 \times 10^{-5}\,\mathrm{s}$, so the pulse is advected by twice its initial width. We use the modified CFL time-step criterion [equation (23)] for this problem, with a CFL number $C_0 = 0.4$.

In Fig. 6, we compare the results of the two runs; for the advected case we have shifted the solution by a distance $v_0 t = 48\,\mathrm{cm}$ in the $-x$ direction, so that it should lie on top of the unadvected case. We see that the agreement between the advected and unadvected solutions is very good. The maximum relative errors are bounded by 0.7 per cent over the domain, and we obtain a relative L_1 norm error of 0.1 per cent. This demonstrates that our scheme is handling the advection of radiation by gas in the diffusion regime appropriately, and provides evidence for the correct modelling of the velocity-dependent radiative work and advection terms in the moment equations.

3.7 Spherical expansion of radiation-pressure dominated H ii region

In our next test, we simulate the radiation pressure-driven expansion of a thin, dusty, spherical shell as given in Skinner & Ostriker (2013) (SO13 hereafter). The problem considers an idealized central source of photons – for example a massive star or star cluster – impinging on a surrounding dusty cloud that absorbs the photons, transferring momentum to the gas. This is a fully coupled radiation-hydrodynamic problem that tests gas-radiation momentum exchange in three dimensions. The central source function for the radiation field is given by

$$j_*(r) = \frac{L_*}{\left(2\pi R_*^2\right)^{3/2}} \exp\left(-\frac{r^2}{2R_*^2}\right), \tag{60}$$

where L_* is the luminosity of the cluster and R_* the size of the source. We add j_* as a source term on the right-hand side of our equation for E_r. In addition, we add the corresponding term $j_*(r)/(4\pi \rho \kappa_P)$ to the source function of the ray tracer, taking into account the contribution of the central source in the computation of the Eddington tensor **T**. The test assumes that at $t = 0$, a shell of thickness H and zero velocity is present at a radius $r = r_0$, and monitors the evolution of the shell radius and velocity with time. The radial density profile at $t = 0$ is given by

$$\rho_{\mathrm{sh}}(r) = \frac{M_{\mathrm{sh}}}{4\pi r^2 \sqrt{2\pi R_{\mathrm{sh}}^2}} \exp\left(-\frac{(r-r_0)^2}{2R_{\mathrm{sh}}^2}\right), \tag{61}$$

where M_{sh} is the gas mass in the thin shell, and $R_{\mathrm{sh}} \equiv H/(2\sqrt{2\ln 2})$ is the half-width of the shell. The dust opacity κ_0 is set to be constant in space and time for simplicity. Following SO13, we define the following quantities to non-dimensionalize the problem setup: a length unit of r_0, density unit $\rho_0 = 3M_{\mathrm{sh}}/(4\pi r_0^3)$, velocity unit a_0 corresponding to the isothermal sound speed, and time unit $t_0 = r_0/a_0$. Under the thin-shell approximation, and assuming reprocessed radiation pressure in the dusty shell to be the only source of radial pressure, it is possible to express the time evolution of the radius of the shell as an analytic parametric equation in these dimensionless units (equation 106 of SO13), given by

$$\tilde{t} = \frac{1}{\mathcal{M}_0\sqrt{2}}\left[\sqrt{\tilde{r}}\sqrt{\tilde{r}-1} + \ln\left(\sqrt{\tilde{r}} + \sqrt{\tilde{r}-1}\right)\right], \tag{62}$$

where $\tilde{t} = t/t_0$, $\tilde{r} = r/r_0$, and $\mathcal{M}_0 = \sqrt{L_*\kappa_0/(4\pi r_0 c a_0^2)}$ is the reference dynamical Mach number. Similarly the shell velocity is given by (equation 105 of SO13)

$$\frac{\mathrm{d}\tilde{r}}{\mathrm{d}\tilde{t}} = \mathcal{M}_0\sqrt{2}\left(1 - \frac{1}{\tilde{r}}\right)^{1/2}. \tag{63}$$

We use these relations to compare with the shell radius and velocity in our simulations below. SO13 simulate the problem with an isothermal equation of state, and under the conditions of radiative equilibrium ($|a_R T^4 - E_r| = 0$) for simplicity, which we also adopt here.

We setup the problem with parameters identical to those specified in SO13: initial shell radius $r_0 = 5\,\mathrm{pc}$, thickness $H = 0.3r_0 = 1.5\,\mathrm{pc}$, central source luminosity $L_* = 1.989 \times 10^{42}\,\mathrm{erg\,s^{-1}}$, central source size $R_* = r_0/8 = 0.625\,\mathrm{pc}$, and dust opacity of $\kappa_P = \kappa_R = \kappa_0 = 20\,\mathrm{cm^2\,g^{-1}}$. The isothermal sound speed is set to $a_0 = 2\,\mathrm{km\,s^{-1}}$, which corresponds to a gas temperature $T \sim 481\,\mathrm{K}$, assuming a mean particle mass $\mu = m_{\mathrm{H}}$. The simulation is performed on the domain $(x, y, z) \in [-10, 10]^3\,\mathrm{pc}$, with the source at $x = y = z = 0$, with outflow boundary conditions on the gas and radiation. We note that SO13 simulate only a quadrant of the sphere with reflecting

boundary conditions at the $x = 0$ boundary, which we did not repeat here to avoid having to implement reflecting boundary conditions in the RT solver used to compute **T**. We use AMR for this test, with a base resolution of 32^3, and allow up to four levels of refinement, corresponding to an effective resolution of 256^3. We refine blocks where $a_0/\sqrt{G\rho} > 16\Delta x$. We note that this is identical to the standard Jeans refinement criteria, but we remind the reader that we do not have self-gravity in this simulation. We also perform simulations on uniform grids of resolution 64^3, 128^3, and 256^{39} to study the dependence of shell evolution on resolution.

While we initialize the density distribution following SO13, we must use a different method to initialize the radiation energy density and flux, due to the difference in closures between VETTAM and SO13's M_1 approach. SO13 initialize the problem with a quasi-static steady state radiation energy density ($E_r^*(r)$) and flux ($F_r^*(r)$), derived under the condition of radiative equilibrium. Specifically, they estimate $F_r^*(r)$ by setting $\partial E_r/\partial t = 0$, which gives

$$\nabla \cdot F_r^* = j_*(r), \tag{64}$$

which can be inverted to obtain

$$F_*(r) = \frac{L_*}{4\pi r^2}\left[\operatorname{erf}\left(\frac{r}{\sqrt{2}R_*}\right) - \frac{2r}{\sqrt{2\pi}R_*^2}\exp\left(-\frac{r^2}{2R_*^2}\right)\right]. \tag{65}$$

Similarly, they obtain the solution for $E_r^*(r)$ by setting $\partial F_r/\partial t = 0$, which gives $\nabla \cdot \mathbf{P} = -\rho\kappa_0 \mathbf{F}/c$, and then invoking the M_1 closure to relate $\mathbf{P}$ to E_r. Since we do not have an analytic closure relation, our alternative approach is to set $E_r = F_r = 0$ as the initial condition, and evolve the system without hydrodynamics for a transient period until the radial profiles of E_r and F_r reach a steady state. We plot the radial profiles of E_r, F_r, and $\nabla \cdot F_r$ obtained at the steady state in our simulation in Fig. 7; we also show the profile of density ρ for reference. We find that $\nabla \cdot F_r$ and F_r are very close to the results given by equations (64) and (65), respectively, indicating that the M_1 approximation is close to our full VET result for this problem. We also verified that the solution converges to this steady state solution from other initial conditions as well.

Once the radiation field has reached steady state, we turn hydrodynamics back on, and allow the system to evolve. We use the unmodified CFL condition to determine the time-step, enforcing a density floor of $\rho_{\min} = 10^{-8}\,\rho_0$ to prevent very small time-steps, and run the simulation to a final time of $t_{\text{final}} = 0.5\,\text{Myr}$. We show slice plots following the evolution of the expanding thin shell for three different times in Fig. 8, with the AMR block structure overplotted. We then estimate the radius of the shell at a given time t by calculating the mass-weighted average radius in our computational domain, given by

$$\langle r \rangle \equiv \frac{\int \rho r \, dV}{\int \rho \, dV}, \tag{66}$$

where $r = \sqrt{x^2 + y^2 + z^2}$ is the radius of a grid point in the domain, ρ the local density, and dV the volume of the cell. In addition, we can also compute the mass-weighted radial velocity as

$$\langle v_r \rangle \equiv \frac{\int \rho(\mathbf{v}\cdot\hat{\mathbf{r}})\,dV}{\int \rho \, dV}, \tag{67}$$

where $\mathbf{v}\cdot\hat{\mathbf{r}}$ denotes the Cartesian velocities projected in the radial direction. We show the time evolution of our computed values of $\langle r \rangle$ and $\langle v_r \rangle$ in Fig. 9 for our fiducial AMR simulation, and the uniform grid versions at different resolutions. These are compared
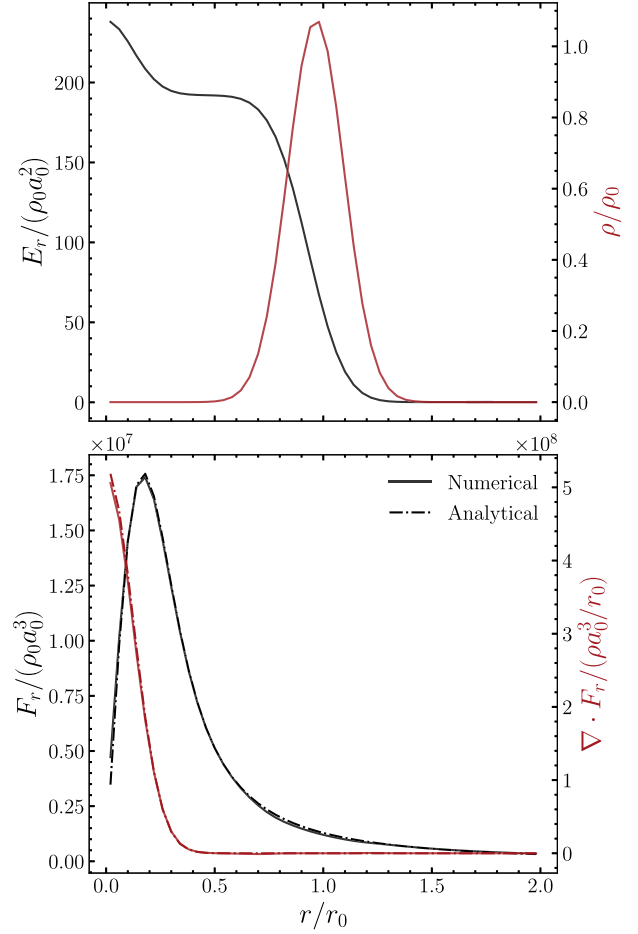
---

[9]SO13 perform their simulations at this resolution

Figure 7. Steady state radial profiles of the radiation energy density E_r (top panel; black), gas mass density ρ (top panel; red), radiation flux F_r (bottom panel; black), and the divergence of the radiation flux $\nabla \cdot F_r$ (bottom panel; red) for the radiation-driven thin shell test without hydrodynamical evolution. The quantities are expressed in the dimensionless units of the problem described in the text. We overplot the analytically derived profiles of $\nabla \cdot F_r$ and F_r given in equations (64) and (65) in the bottom panel with dot–dashed lines, and verify that our solutions are in agreement with them. These profiles represent the initial conditions for the subsequent dynamical evolution of the shell (see text for details).

with the analytical relations for the shell radius and velocity evolution given by equations (62) and (63), respectively. We find excellent agreement at all resolutions, although, as expected, better agreement at higher resolutions. The maximum error in the solutions for the radius (velocity) are bounded by 3.7 per cent (5 per cent), 2.1 per cent (2.2 per cent), and 1.4 per cent (1.9 per cent) for the uniform grid 64^3, 128^3, and 256^3 versions, respectively. The maximum errors in the 256^3 effective resolution AMR version are 1.3 per cent and 1.8 per cent for the radius and velocity respectively, which is comparable to the errors obtained by the 256^3 uniform run. However, we find that the AMR run uses about 30 per cent less CPU time than the uniform grid run, and is thus more efficient.

3.8 Shadow tests

Shadow tests in various forms are commonly used to investigate how well RHD schemes reproduce and preserve angular variations in the radiation field in the presence of a mixture of optically thin and thick
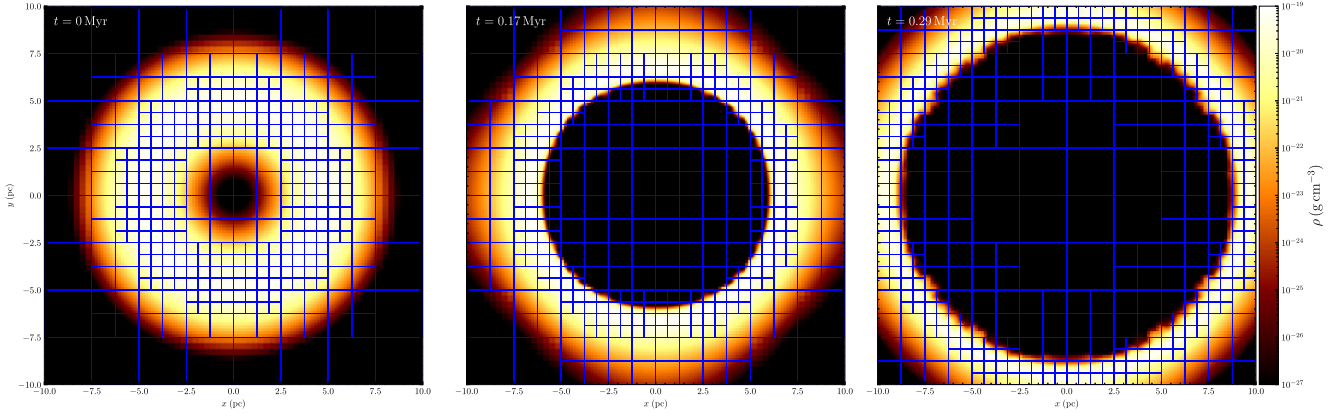
Figure 8. Slice plots of the gas density ρ at times $t = 0, 0.17$ and 0.29 Myr for the radiation-driven shell evolution test simulation, with the block structure of the AMR domain overplotted.
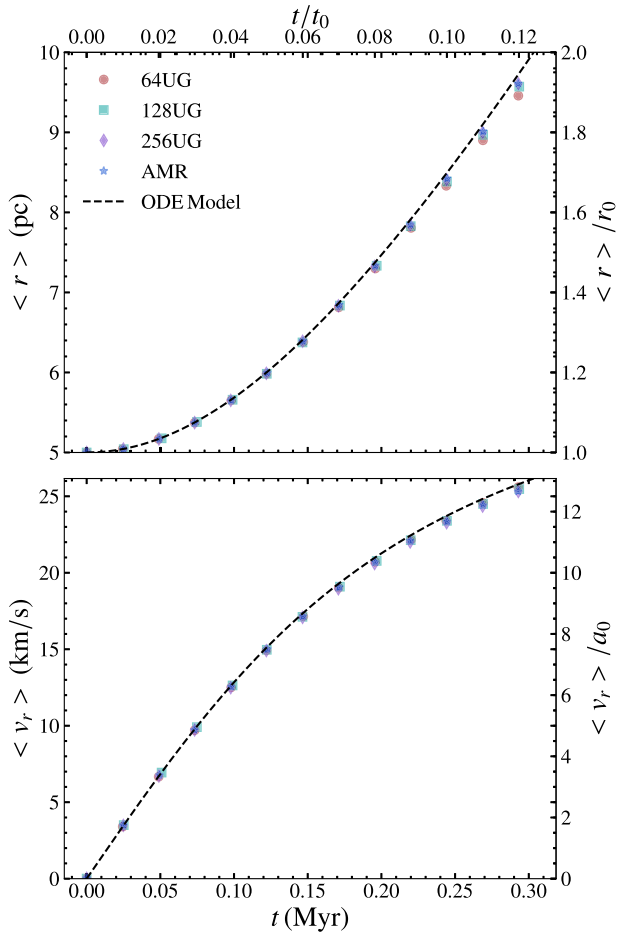

Figure 9. Evolution of the mass-weighted average radius $\langle r \rangle$ (equation (66); top) and radial velocity $\langle v_r \rangle$ (equation (67); bottom) obtained for the radiation-driven thin shell expansion test at regular time intervals, and compared at different resolutions. In addition, we plot the analytical solutions for $\langle r \rangle$ and $\langle v_r \rangle$ from the ODE model of Skinner & Ostriker (2013) for comparison.

gas, and to illustrate the varying levels of directional accuracy that different closure methods achieve. For instance, it is well known that methods based on the diffusion approximation ($\mathbf{P} = (1/3)E_r\mathbf{I}$) fail to cast shadows. Local closures such as the M_1 approximation fail

to propagate the radiation field correctly in the presence of multiple sources of radiation (or effectively, convergent rays) in an optically thin medium (as demonstrated in tests by Rosdahl et al. 2013; Kannan et al. 2019). We perform three forms of shadow test below to demonstrate that our nonlocal VET-closed scheme can cast shadows correctly, even in situations where other methods fail. Hydrodynamic evolution is switched off in all three shadow tests (i.e. $\mathbf{v} = 0$).

In our first version, we perform a test similar to that first presented in Rijkhorst et al. (2006), and recently shown by Klassen et al. (2014) and Rosen et al. (2017), to demonstrate the shadow cast by an optically thick cloud in an optically thin medium when irradiated by two point sources of radiation, where the point source contributions are handled by a ray tracer, and the subsequent diffuse re-emission with the moment method. We show this as a demonstration of the workings of our hybrid radiation algorithm described in Section 2.2.6. While this is a useful problem for testing the coupling between the point and diffuse sources of radiations, the setup of the test is such that the direct irradiation on the clump is the agent that casts the shadow, whereas the moment method is only used for the diffuse re-emission that is largely isotropic. In other words, the presence of the shadow in this case is largely insensitive to the closure for the moment method adopted.

With this in mind, in the next two versions, we instead model setups with solely diffuse sources of radiation that are handled by the moment method only. This is important to test, because in a dynamical simulation, there can self-consistently arise sources of radiation that cannot be reduced to a point source (or sink particle) – for instance, heated overdensities in a clumpy, dusty medium – and whose contribution to the energy budget of the gas could be significant. While the geometric distributions of diffuse sources could be quite general in a dynamical simulation, we consider only simple cases here. For our first test with diffuse sources, we use a modified version of the hybrid radiation test setup, but with the point sources replaced by diffuse spherical sources of radiation modelled by a Gaussian source term. This should, qualitatively, cast a shadow similar to the hybrid radiation test, if the moment method used can handle the propagation of radiation in such a setup correctly. We show that our method passes this test in Section 3.8.2. Following that, in Section 3.8.3, we present a test where we replace the point sources with an extended, non-spherical source of radiation that might be representative, for example, of emission from a hot, clumpy, filament in an otherwise
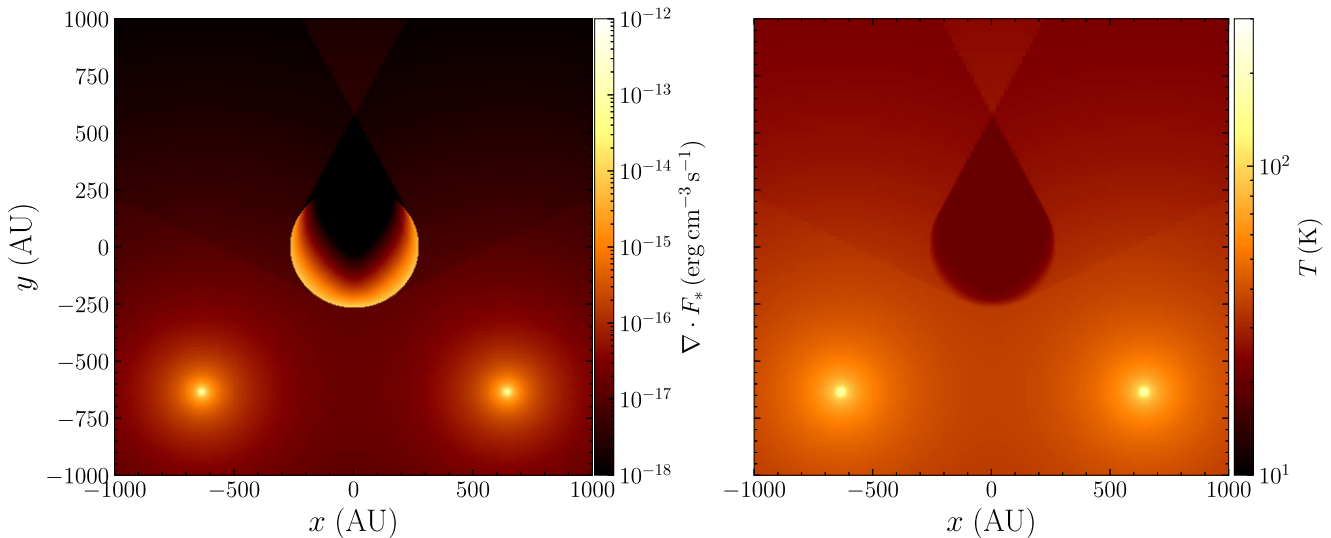
Figure 10. Slice plot of the heating rate per unit volume $\nabla \cdot F_*$ (left) from two-point sources of luminosity $L_* = 1\,L_\odot$ irradiating an optically thick clump, and the resulting gas temperature T (right) obtained through absorption and subsequent re-emission of this energy. This test demonstrates the working of our hybrid RT scheme (see Section 3.8.1).

optically thin medium, or from a geometrically thin accretion disc in an optically thin atmosphere. We again show that a qualitatively correct shadow is obtained with our scheme for this setup. We elaborate on the test setups, and show the results we obtain, below.

3.8.1 Hybrid radiation with point sources

First, we perform a test with the hybrid radiation algorithm to demonstrate that the coupling between the direct radiation field modelled with the ray tracer, and the reprocessed radiation that we handle using the VET closure is implemented correctly. To setup this test, we place a dense clump of material at the centre of a $(2000\,\mathrm{AU})^3$ computational domain, with radius 267 AU and density $\rho_c = 3.89 \times 10^{-17}\,\mathrm{g\,cm^{-3}}$. The clump is surrounded by an optically thin ambient medium with density $\rho_a = 3.89 \times 10^{-20}\,\mathrm{g\,cm^{-3}}$. The gas temperature is taken to be spatially uniform with a value of 20 K. The clump is irradiated by two point sources of solar luminosity (i.e. $1\,L_\odot$) placed 368 AU from the edges of the clump at $(x, y, z) = (\pm 635, -635, 0)$ AU. The opacity for the direct stellar radiation is set to $\kappa_* = 64\,\mathrm{cm^2\,g^{-1}}$, whereas the moment method uses the grey opacities from Semenov et al. (2003). We use AMR for this test, discretizing the grid with a base resolution of 128^3, and refine the grid based on the modified second derivative condition in FLASH (Fryxell et al. 2000) on the variables E_r and ρ, up to a maximum resolution of 512^3. In addition, we ensure that the dense clump is always refined to the maximum resolution. We use 48 angles for the ray tracer, although we found that our results were insensitive to this choice.

In Fig. 10, we show the irradiation from the direct field from point sources (left), and the subsequent gas temperature obtained after this is reprocessed by the gas and it cools. As we can see, our point-source irradiation produces a clear shadow, whereas the diffuse re-emission works to smoothen the temperature field. This test shows that our hybrid approach of coupling the contribution of radiation from point sources and the diffuse emission works correctly.

3.8.2 Spherical diffuse sources

To demonstrate that our VET method is capable of capturing shadows even in the presence of purely diffuse sources of radiation, we setup a modified version of the test described in the previous section. The primary modification we make is to replace the point sources of radiation with diffuse sources, modelled with a Gaussian source function $j_*(r)$ with a profile identical to that given in equation (60). We add this as a source term for our equation of E_r in our VET scheme. We use a value of $L_* = 10\,L_\odot$ and $R_* = 54$ AU for both the sources. We also change the positions of the sources with respect to the previous test such that they are 90^{deg} apart with respect to each other, at $(635, 0, 0)$ AU and $(0, 635, 0)$ AU, respectively. We make this change simply to prevent confusion with the test described in the previous version. In addition, for simplicity, we set the diffuse radiation opacities to be independent of the gas state with a constant value of $\kappa_P = \kappa_R = 100\,\mathrm{cm^2\,g^{-1}}$. This constant value ensures that the clump is optically thick to the diffuse radiation, whereas the ambient medium is optically thin to it. We use a base grid resolution of 128^3 for this test, and refine based on the modified second derivative condition in FLASH (Fryxell et al. 2000) on the variables ρ and j_*, up to a maximum resolution of 512^3, which ensures that the sources and the edges of the clump are well resolved. In addition, we use a total of 192 angles for the ray tracer while calculating the VET. In Fig. 11, we show a slice plot of the temperature structure obtained with our scheme at a time corresponding to a light crossing time of the box. We can see that a clear shadow is cast by the optically thick clump. We point out that this is a challenging test due to the presence of converging rays of radiation, and local closure methods would fail to propagate the radiation correctly in such a setup, as we shall demonstrate in Section 4.1.

3.8.3 Extended diffuse source

In our final version of the shadow test, we introduce an extended source of diffuse radiation, geometrically represented by a cylinder enclosed by half-spheres at both ends of its axis. We represent this
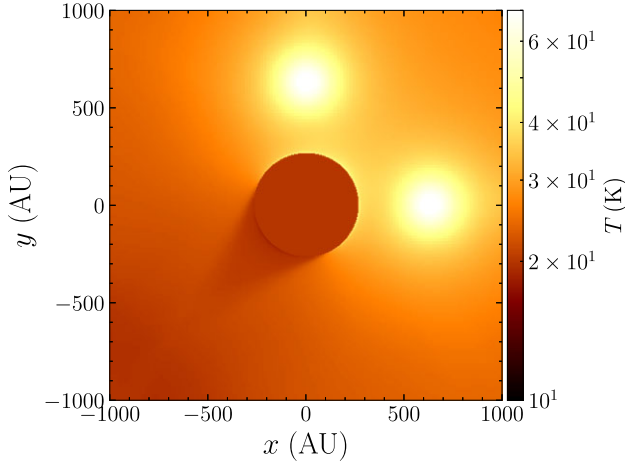
Figure 11. Slice plot of the gas temperature T at a time corresponding to one crossing time of the computational box, demonstrating the shadow cast by two diffuse spherical sources of radiation impinging on an opaque clump of gas, lying in an optically thin ambient medium (see Section 3.8.2).

source by the function

$$
j_* = \begin{cases} j_0 \exp\left[-\left(\frac{y_c^2 + z_c^2}{2R_*^2}\right)\right] & |x_c| \le l_{\mathrm{cyl}},\ \sqrt{y_c^2 + z_c^2} \le 4R_* \\ j_0 \exp\left[-\left(\frac{x_c^2 + y_c^2 + z_c^2}{2R_*^2}\right)\right] & |x_c| > l_{\mathrm{cyl}},\ \sqrt{x_c^2 + y_c^2 + z_c^2} \le 4R_* \\ 0 & \text{All other } (x, y, z) \end{cases}
$$

$$(68)$$

where (x_c, y_c, z_c) are the coordinates with respect to the centre of the source at $(0, -1000, 0)$ AU, $R_* = 27$ AU is the characteristic size of the source, and $j_0 = L_*/(2\pi R_*^2)^{3/2}$ where we pick a value of $L_* = 10\,L_\odot$. The initial conditions for the opaque clump and ambient medium, and the fixed opacity value, are identical to those in the previous test. However, compared to this test, we double the size of the computational volume to 4000 AU in the x and y directions, in order to follow the shadow for longer times; we leave the domain size in the z direction unchanged, at 2000 AU. We use AMR for this test, discretizing the grid with a base resolution of $128 \times 128 \times 64$, and refining up to a maximum resolution of $1024 \times 1024 \times 512$. We use a refinement condition wherein blocks are tagged for refinement if a cell in the block has a relative change $\Delta f \ge 0.8$, where $\Delta f = \max(\Delta f_x, \Delta f_y, \Delta f_z)$, and -

$$
\Delta f_i = \frac{|f(i+1) - f(i-1)|}{|f(i+1) + f(i-1)|},
$$

$$(69)$$

where f is the variable used for refinement, for which we use ρ and j_*, and i is the discretized cell index in the i'th direction where $i \in (x, y, z)$. We use 192 rays in the ray tracer, though we obtain qualitatively identical results with 48 rays. We show the gas temperature evolution for this test in Fig. 12, at times corresponding to 25 per cent, 50 per cent, and 100 per cent of the light crossing time of the computational volume. We can see that the optically thick clump casts a shadow when irradiated by the extended source, and our scheme is able to capture this challenging configuration of multiple converging rays quite well. We also note that subtle shadow features, such as the umbra, penumbra, and antumbra, are noticeable, and is a testament to the ability of our scheme to handle nontrivial geometrical distributions of radiation sources.

4 DISCUSSION

4.1 Comparison to FLD and M_1 schemes

The primary advantage that the scheme described in this paper offers over many other moment method-based schemes is that we use a non-local closure based on the VET obtained with a global ray-trace solution of the time-independent RT equation. The VET closure, in principle, can handle any geometrical arrangements of sources whereas local closure methods fail to propagate radiation correctly in certain situations. It is therefore interesting to compare the performance of our VET scheme to two local closures commonly used in astrophysical codes: the FLD (also known as the Eddington approximation) and Moment-1 (M_1) closures.

To demonstrate the advantage of the VET over these local closures in complex radiation field geometries, we repeat the shadow test with spherical diffuse sources described in Section 3.8.2, with the FLD and M_1 closures, and compare the results to those obtained with the VET. This setup contains multiple sources interacting in an optically thin medium, and subsequently casting a shadow, and hence represents a geometrical setup where local closures are expected to fail. To mimic the Eddington approximation, we set $\mathbf{T} = (1/3)\mathbf{I}$, where $\mathbf{I}$ is the identity tensor. This is technically not identical to the FLD method, since we are still solving the equation for $\mathbf{F}_r$, rather than determining it from the instantaneous distribution of E_r; however the results are expected to be qualitatively identical. To mimic the M_1 closure, we set

$$
\mathbf{T} = \frac{1-\chi}{2}\mathbf{I} + \frac{3\chi - 1}{2}\hat{\boldsymbol{n}}\hat{\boldsymbol{n}},
$$

$$(70)$$

where $\hat{\boldsymbol{n}} = \boldsymbol{F}_r/\|\boldsymbol{F}_r\|$ is the unit vector in the direction of the radiation flux and χ is the Eddington factor given by

$$
\chi(f) = \frac{3 + 4f^2}{5 + 2\sqrt{4 - 3f^2}},
$$

$$(71)$$

where $f = \boldsymbol{F}_r/(cE_r)$. We compute the components of $\mathbf{T}$ with the relations above using the value of E_r and $\boldsymbol{F}_r$ at the beginning of the time-step (i.e. time-lagged). We show the comparison of the temperature structure after one light crossing time obtained with the three closures in Fig. 13. We can see that the Eddington and M_1 closure versions do not cast qualitatively correct shadows, whereas the VET version does. This demonstrates that the VET is the only closure relation that ensures the consistent propagation of radiation in non-trivial geometrical distributions of diffuse radiation sources in the presence of optically thin media.

This leads to the important question of whether such differences could be dynamically relevant in a scientific application. This would clearly depend on the problem simulated and the potential presence of a mixture of transparent and opaque media, keeping in mind that a *formal* comparison of different closure methods for a realistic numerical setup has not been performed to our knowledge. That said, the well-studied problem of a wind by trapped infrared radiation, in a gaseous atmosphere confined by a constant gravitational acceleration, could serve as a qualitative tool of comparison.

First investigated by Krumholz & Thompson (2012) with the FLD closure, this setup has been reattempted with the M_1 (Rosdahl & Teyssier 2015) and VET (Davis et al. 2014) closures, and also with methods that do not rely on angular moments of the transfer equation, such as Monte Carlo Radiation Transport (MCRT; Tsang & Milosavljević 2015; Smith et al. 2020) and implicit solutions of the time-dependent RT equation (Jiang 2021). While there are broad similarities in the gas evolution with various closures, in
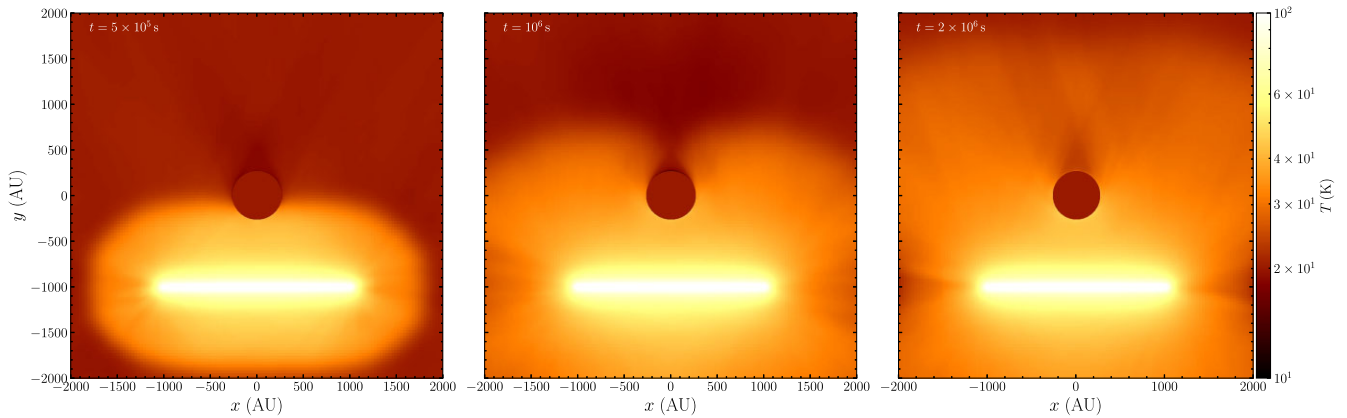
Figure 12. Time evolution of the gas temperature T of an optically thick clump placed in a transparent medium, irradiated by an extended source of radiation (equation (68)). Times correspond to 25 per cent, 50 per cent, and 100 per cent of the light crossing time of the computational volume. Our scheme is able to capture the shadow cast by the clump very well, including subtle features such as the umbra, penumbra, and antumbra.
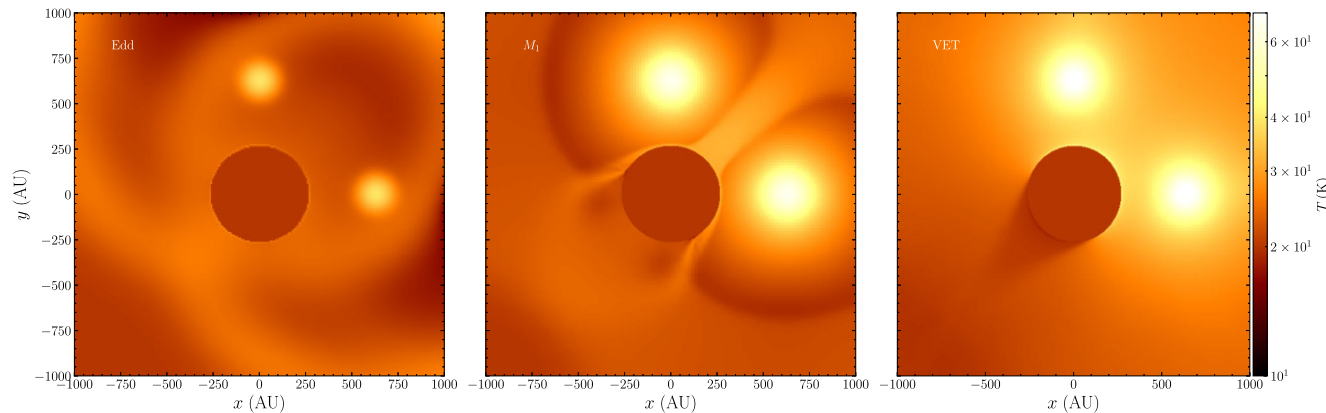

Figure 13. The numerical solution to the shadow test obtained by adopting different closures. All panels show gas temperature as a function of position at a time corresponding to one light crossing time of the computational box. The left-most panel shows the solution obtained using the FLD (or Eddington) closure, the middle panel shows the M_1 closure, and the right-hand panel shows our VET result.

that all schemes find that the system rearranges itself to reduce momentum transfer between radiation and gas such that the effective Eddington ratio drops from its initial value of $\sim$50 to very close to unity, the FLD and M_1 closure simulations find that the steady-state Eddington ratio is slightly below unity, such that in steady state the gas remains gravitationally confined without driving a wind. On the other hand, the VET and non-moment based methods[10] (which are expected to be at least as accurate as the VET) find that the asymptotic Eddington ratio is slightly larger than unity, leading to a slowly accelerated wind. This suggests that, in certain problems, adopting a non-local closure and/or accurate model of radiation propagation leads to qualitatively different outcomes for the dynamical evolution of gas. There is a significant scope for further work to identify, compare, and quantify differences in astrophysically relevant simulation setups with the adopted treatment of radiation transport.

---

[10]We note that Smith et al. (2020) compare their MCRT result with an M_1 closure relation version that shares the same hydrodynamics solver, and find similar discrepancies, suggesting that the adopted model for radiation transport is probably what drives the differences between these studies.

4.2 Performance

The computational cost of VETTAM is very problem dependent, because the convergence of the sparse matrix solvers and the fixed-point iterations depend on the physical state of the system (κ and T distributions), which determines the stiffness of the matrix, and on the distribution of adaptive grids to MPI ranks, which determines the amount of non-local communication required. In addition, the overall performance of our scheme is highly dependent on the performance of the (i) hybrid characteristics ray tracer, for which performance and scaling capabilities are provided in Buntemeyer et al. (2016), and (ii) solvers in the external PETSc library, whose performance is not directly under the control of VETTAM, apart from the choice of solver, pre-conditioner, and solver tolerance set by the user, which in certain problems can be very important. Due to these external dependencies, we do not elaborate on formal performance or scaling tests for our scheme, but rather, briefly discuss certain points relevant to performance in our scheme.

In an RHD simulation, we have found that VETTAM occupies the largest share of computational cost. For instance, in the full RHD simulation setup of Section 3.7, VETTAM was $\sim$10 times more expensive than the hydrodynamics update per evolution step.
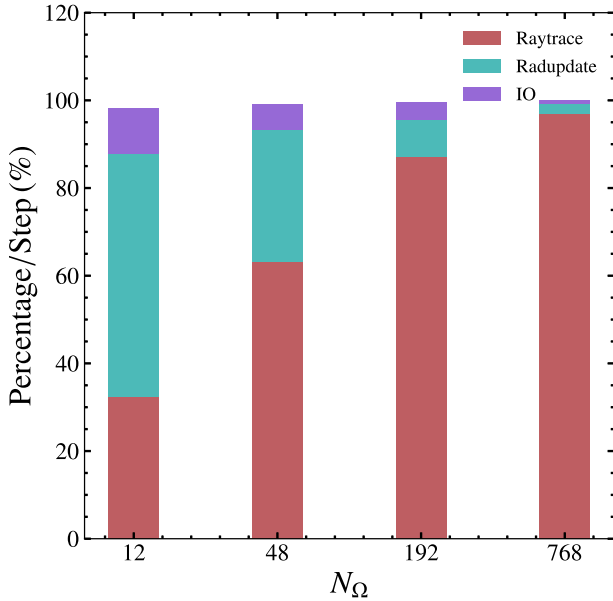
Figure 14. Breakdown of wallclock times used in the three most time-consuming units for the shadow test of Section 3.8.2, as a function of the number of angles N_Ω used in the ray trace. We can see that the ray tracer occupies the largest fraction of the cost, and increasingly so at higher angular resolution.

However, this is again very problem dependent and this value can be higher or lower for a different problem. In general we have found the ray tracer to be the primary bottleneck to performance, though the extent to which it dominates the cost depends on the choice of angular resolution. We quantify this by running the shadow test described in Section 3.8.2 on 144 cores, which corresponds to three compute nodes.[11] In Fig. 14, we show the breakdown of time spent by the three most time-consuming units in the simulation – compared for different angular resolutions for the ray tracer (see Appendix B for a comparison of results obtained for them). Since hydrodynamics was switched off for this test, it does not enter the cost breakdown. We see that even with modest angular resolutions of 48 rays, the ray tracer constitutes ~ 60 per cent of the computing cost, whereas the implicit radiation update represents only ~ 30 per cent; the dominance of the ray tracing step rises sharply at higher angular resolution. Thus, for science applications with VETTAM, we expect the ray tracer to be the most expensive part of the simulation. For certain problems, we speculate that it might be possible to consider updating the Eddington tensor every few simulation time-steps, rather than at the beginning of *every* timestep, without it affecting the solution significantly. This is a potential approach to alleviate the overall computational cost of the scheme in an application.

Another difficulty associated with the ray tracer has to do with its limited parallel efficiency due to inherent communication needs. This limits the strong scaling efficiency of the scheme, as the communication overheads quickly result in lower parallel efficiency, if the problem size remains fixed (see, Buntemeyer et al. 2016, for

---

[11] All tests relevant to this section were performed on the Gadi supercomputer at the National Computational Infrastructure (NCI), Australia. Each node contains 2 x 24-core Intel Xeon Platinum 8274 (Cascade Lake) processors with 3.2 GHz CPUs per node and 192 GB of RAM, interconnected with HDR Infiniband technology in a Dragonfly+ topology.
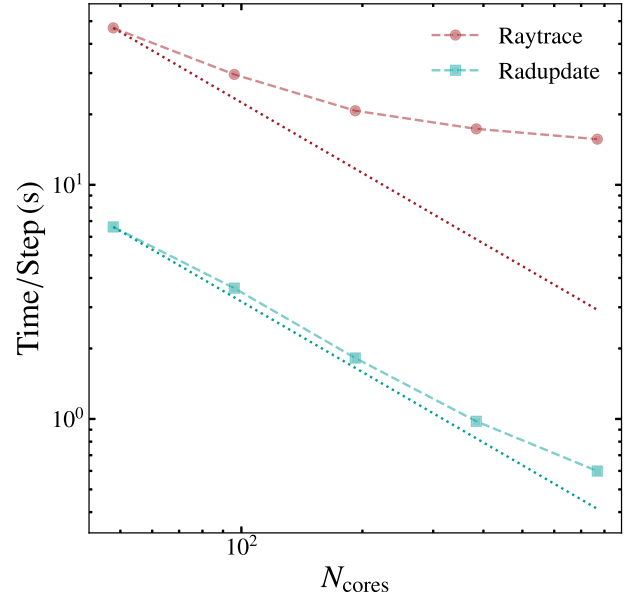
Figure 15. Strong scaling performance for the ray tracing and implicit radiation updates performed by VETTAM in each simulation time-step for the shadow test of Section 3.8.2, with $N_\Omega = 192$. We find reasonable strong scaling for the radiation update, but relatively poor scaling for the ray-trace step due to associated communication overheads (see Buntemeyer et al. 2016).

a discussion on this). To quantify the scaling behaviour, we repeat the shadow test of Section 3.8.2 with varying number of processors, keeping the AMR block structure – and hence the total computational load – fixed. We found in our tests that the implicit radiation moment equations update performs reasonably in strong scaling out to 768 cores, especially considering that the sparse matrix solvers have communication overheads as well. The times per evolution step in the strong scaling test for the ray trace and the radiation update are shown in Fig. 15. This indicates that there is a careful choice to be made by the user to ensure that the number of blocks occupied by each processor in a parallel simulation is high enough for communication overheads not to dominate the total cost, and at the same time low enough that it satisfies the memory requirements of the ray tracer. We aim to test, monitor, and improve the performance characteristics of the scheme in the future.

4.3 Caveats

In this section, we briefly mention some caveats associated with our implementation, and provide motivation for future work when applicable.

(i) Our scheme is limited to the grey approximation, and this limits the usage of the scheme to problems where the spectral dependence of the radiation field is not expected to be crucial. It is, however, possible to extend our scheme with a multigroup moment method (Vaytet et al. 2011), and this a direction for future work.

(ii) The VET is computed only once at the beginning of the time-step with the ray-trace solution of the time-independent transfer equation. However, this would not be appropriate for systems where the radiation field changes substantially on time-scales much smaller than a hydrodynamic time step, so that the Eddington tensor computed at the beginning of a time-step is a poor guess for its value at the end of the step. In principle, one could handle such systems by iterating the Eddington tensor to convergence, along with the

other radiation quantities. However, this is likely computationally intractable, and it is unclear whether it would be accurate in any event – an accurate solution would likely require choosing a time-step small enough to capture the time evolution of the radiation field.

(iii) The Picard iteration scheme achieves only linear convergence, and thus the number of iterations required can be very dependent on the initial starting guess. An extension would be to implement a method to accelerate convergence, such as Anderson acceleration, or to solve the nonlinear system with a Jacobian-free Newton Krylov method; both achieve up to quadratic rates of convergence. That being said, Picard iteration generally has a greater radius of convergence compared to Newton methods. At present, there is little reason to optimize the iterative solve, since the total cost is dominated by the ray trace, but as we improve the ray trace and relieve this constraint, we also intend to improve the iterative scheme.

(iv) VETTAM solves the equations of RHD in the mixed frame formulation by expanding the lab frame opacities in terms of the comoving frame opacities to $\mathcal{O}(v/c)$ (Mihalas & Klein 1982). This formulation is poorly suited to line radiation transport, and hence we are limited to continuum radiation.

(v) Our scheme is first order in space and time, and while this maintains stability and simplicity, it can be diffusive in certain problems due to the associated truncation errors (for instance in Section 3.1 for the streaming regime). A direction for future work would be the development of higher-order implicit Godunov methods to treat the RHD equations that resolves the associated difficulties of maintaining monotonicity in an implicit higher-order method (for a discussion, see Section 4.2, Sekora & Stone 2010).

5 SUMMARY

In this paper we describe VETTAM, a multidimensional RHD algorithm that solves the mixed-frame radiation moment equations closed with a non-local VET computed through a formal solution of the time-independent RT equation. VETTAM is, to our knowledge, the first ever implementation of a VET closure scheme that can handle AMR. We have coupled our implementation to our own private version of the FLASH hydrodynamics code (Fryxell et al. 2000), which uses the PARAMESH library for AMR (MacNeice et al. 2000). Our scheme has been designed to handle continuum radiation transport mediated by dust, although other radiative mechanisms, such as photoionization (e.g. Aubert & Teyssier 2008; Kuiper, Yorke & Mignone 2020), or alternative transport phenomena such as cosmic ray or neutrino transport, can be performed with slight modifications (e.g. Jiang & Oh 2018). We use a finite-volume Godunov method with an HLLE Riemann solver for the radiation moment equations with an implicit backwards-Euler time update that allows us to evolve the system at the hydrodynamic time-scale. In addition, we treat the coupled nonlinear radiation-matter energy exchange term through a fixed-point Picard iteration method, whicgh effectively linearizes the backwards-Euler update, for which we use the sparse matrix solving capability provided by the PETSc library. The formal solution to the time-independent transfer equation for computing the VET is performed through the hybrid characteristics ray-tracing scheme implemented by Buntemeyer et al. (2016). We carry out a comprehensive suite of tests to demonstrate that our scheme works correctly in different regimes of radiation transport, and can handle the coupling between radiation and hydrodynamics correctly. We also demonstrate through a test that other commonly used local closure methods such as FLD or M_1 yield unphysical radiation fields in certain physical scenarios, the dynamical effects of which are difficult to predict and poorly explored (e.g. Davis et al. 2014). However,

implicit VET methods are computationally more expensive than other closures due to the inherent communication needs of the ray-tracing scheme and matrix inversion algorithms. We argue, however, that the computational cost benefits offered by AMR in our scheme will be crucial in applications that require both spatial accuracy and computational efficiency. Currently, we are using VETTAM to study the effects of reprocessed infrared radiation pressure on super-star cluster formation in dense molecular clouds (e.g. Skinner & Ostriker 2015; Tsang & Milosavljević 2018), and intend to explore other relevant applications in the near future.

Software: PETSC (Balay et al. 1997, 2021), NUMPY (Harris et al. 2020), SCIPY (Virtanen et al. 2020), MATPLOTLIB (Hunter 2007), and YT (Turk et al. 2010). This research has made use of NASA's Astrophysics Data System (ADS) Bibliographic Services.

DATA AVAILABILITY

No new data were produced from this study. VETTAM has been implemented in our own private forked version of FLASH, and would be shared on reasonable request to the corresponding author.

REFERENCES

Asahina Y., Takahashi H. R., Ohsuga K., 2020, ApJ, 901, 96
Aubert D., Teyssier R., 2008, MNRAS, 387, 295
Audit E., Charrier P., Chièze J. P., Dubroca B., 2002, preprint (arXiv:astro–ph/0206281)
Balay S., Gropp W. D., McInnes L. C., Smith B. F., 1997, in Arge E., Bruaset A. M., Langtangen H. P., eds, Modern Software Tools in Scientific Computing. Birkhäuser Press, Boston, MA, p. 163
Balay S. et al., 2021, Technical Report ANL-21/39 - Revision 3.16, PETSc/TAO Users Manual, Argonne National Laboratory
Berger M. J., Colella P., 1989, J. Comput. Phys., 82, 64
Bitsch B., Crida A., Morbidelli A., Kley W., Dobbs-Dixon I., 2013, A&A, 549, A124
Bloch H., Tremblin P., González M., Padioleau T., Audit E., 2021, A&A, 646, A123
Buntemeyer L., Banerjee R., Peters T., Klassen M., Pudritz R. E., 2016, New Astron., 43, 49

Burden R. L., Faires J. D., 1997, Numerical Analysis. Brooks/Cole Publishing Company, Pacific Grove, California

Castor J. I., 2004, Radiation Hydrodynamics. Cambridge Univ. Press, Cambridge

Castor J. I., 2009, in Hubeny I., Stone J. M., MacGregor K., Werner K., eds, AIP Conf. Ser. Vol. 1171, American Institute of Physics Conference Series. p. 230

Castor J. I., Abbott D. C., Klein R. I., 1975, ApJ, 195, 157

Chan T. K., Theuns T., Bower R., Frenk C., 2021, MNRAS, 505, 5784

Chatzopoulos E., Weide K., 2019, ApJ, 876, 148

Commerçon B., Teyssier R., Audit E., Hennebelle P., Chabrier G., 2011, A&A, 529, A35

Commerçon B., Debout V., Teyssier R., 2014, A&A, 563, A11

Courant R., Friedrichs K., Lewy H., 1928, Math. Ann., 100, 32

Davis S. W., Tchekhovskoy A., 2020, ARA&A, 58, 407

Davis S. W., Stone J. M., Jiang Y.-F., 2012, ApJS, 199, 9

Davis S. W., Jiang Y.-F., Stone J. M., Murray N., 2014, ApJ, 796, 107

Dubey A., Reid L. B., Fisher R., 2008, Phys. Scr., 132, 014046

Dubey A., Tzeferacos P., Lamb D. Q., 2019, Int. J. High Perform. Comput. Appl., 33, 322

Federrath C., Banerjee R., Clark P. C., Klessen R. S., 2010, ApJ, 713, 269

Flock M., Fromang S., González M., Commerçon B., 2013, A&A, 560, A43

Fryxell B. et al., 2000, ApJS, 131, 273

Gehmeyr M., Mihalas D., 1994, Physica Nonlinear Phenom., 77, 320

Gittings M. et al., 2008, Comput. Sci. Discov., 1, 015005

Gnedin N. Y., Abel T., 2001, New Astron., 6, 437

González M., Audit E., Huynh P., 2007, A&A, 464, 429

Harries T. J., 2015, MNRAS, 448, 3156

Harris C. R. et al., 2020, Nature, 585, 357

Hayes J. C., Norman M. L., 2003, ApJS, 147, 197

Howell L. H., Greenough J. A., 2003, J. Comput. Phys., 184, 53

Hunter J., 2007, Comput. Sci. Eng., 9, 90

Janka H.-T., Langanke K., Marek A., Martínez-Pinedo G., Müller B., 2007, Phys. Rep., 442, 38

Jiang Y.-F., 2021, ApJS, 253, 49

Jiang Y.-F., Oh S. P., 2018, ApJ, 854, 5

Jiang Y. F., Stone J. M., Davis S. W., 2012, ApJS, 199, 14

Jiang Y.-F., Stone J. M., Davis S. W., 2013, ApJ, 767, 148

Kannan R., Vogelsberger M., Marinacci F., McKinnon R., Pakmor R., Springel V., 2019, MNRAS, 485, 117

Kelley C., 1995, Iterative Methods for Linear and Nonlinear Equations. Frontiers in Applied Mathematics. Society for Industrial and Applied Mathematics, Philadelphia, Google books

Klassen M., Kuiper R., Pudritz R. E., Peters T., Banerjee R., Buntemeyer L., 2014, ApJ, 797, 4

Knoll D., Keyes D., 2004, J. Comput. Phys., 193, 357

Kolb S. M., Stute M., Kley W., Mignone A., 2013, A&A, 559, A80

Krumholz M. R., Thompson T. A., 2012, ApJ, 760, 155

Krumholz M. R., Klein R. I., McKee C. F., Bolstad J., 2007a, ApJ, 667, 626

Krumholz M. R., Stone J. M., Gardiner T. A., 2007b, ApJ, 671, 518

Krumholz M. R., McKee C. F., Bland-Hawthorn J., 2019, ARA&A, 57, 227

Kuiper R., Klessen R. S., 2013, A&A, 555, A7

Kuiper R., Klahr H., Dullemond C., Kley W., Henning T., 2010, A&A, 511, A81

Kuiper R., Klahr H., Beuther H., Henning T., 2012, A&A, 537, A122

Kuiper R., Yorke H. W., Mignone A., 2020, ApJS, 250, 13

LeVeque R. J., 2002, Finite Volume Methods for Hyperbolic Problems. Cambridge Texts in Applied Mathematics. Cambridge Univ. Press, Cambridge

Levermore C. D., 1984, J. Quant. Spectrosc. Radiat. Transfer, 31, 149

Levermore C. D., Pomraning G. C., 1981, ApJ, 248, 321

Lohner R., 1987, Comput. Methods Appl. Mech. Eng., 61, 323

Lowrie R. B., Edwards J. D., 2008, Shock Waves, 18, 129

Lowrie R. B., Rauenzahn R. M., 2007, Shock Waves, 16, 445

Lowrie R. B., Morel J. E., Hittinger J. A., 1999, ApJ, 521, 432

MacNeice P., Olson K. M., Mobarry C., de Fainchtein R., Packer C., 2000, Comput. Phys. Commun., 126, 330

Marshak R. E., 1958, Phys. Fluids, 1, 24

Melon Fuksman J. D., Klahr H., Flock M., Mignone A., 2021, ApJ, 906, 78

Mignon-Risse R., González M., Commerçon B., Rosdahl J., 2020, A&A, 635, A42

Mihalas D., 1978, Stellar Atmospheres. W.H. Freeman, San Francisco

Mihalas D., Auer L., 2001, J. Quant. Spectrosc. Radiat. Transfer, 71, 61

Mihalas D., Klein R. I., 1982, J. Comput. Phys., 46, 97

Mihalas D., Mihalas B. W., 1984, Foundations of radiation hydrodynamics. Oxford University Press, New York

Minerbo G. N., 1978, J. Quant. Spectrosc. Radiat. Transfer, 20, 541

Moens N., Sundqvist J. O., El Mellah I., Poniatowski L., Teunissen J., Keppens R., 2021, A&A, 657, A81

Murray S. D., Castor J. I., Klein R. I., McKee C. F., 1994, ApJ, 435, 631

Naab T., Ostriker J. P., 2017, ARA&A, 55, 59

Peters T., Banerjee R., Klessen R. S., Mac Low M.-M., Galván-Madrid R., Keto E. R., 2010, ApJ, 711, 1017

Pomraning G. C., 1973, The Equations of Radiation Hydrodynamics. Pergamon Press, Oxford

Ramsey J. P., Dullemond C. P., 2015, A&A, 574, A81

Rijkhorst E. J., Plewa T., Dubey A., Mellema G., 2006, A&A, 452, 907

Rosdahl J., Teyssier R., 2015, MNRAS, 449, 4380

Rosdahl J., Blaizot J., Aubert D., Stranex T., Teyssier R., 2013, MNRAS, 436, 2188

Rosen A. L., Krumholz M. R., McKee C. F., Klein R. I., 2016, MNRAS, 463, 2553

Rosen A. L., Krumholz M. R., Oishi J. S., Lee A. T., Klein R. I., 2017, J. Comput. Phys., 330, 924

Rosen A. L., Offner S. S. R., Sadavoy S. I., Bhandare A., Vázquez-Semadeni E., Ginsburg A., 2020, Space Sci. Rev., 216, 62

Saad Y., 2003, Iterative Methods for Sparse Linear Systems, 2nd ed. Society for Industrial and Applied Mathematics, Philadelphia, available at Google books

Saad Y., Schultz M. H., 1986, SIAM J. Sci. Stat. Comput., 7, 856

Sekora M. D., Stone J. M., 2010, J. Comput. Phys., 229, 6819

Semenov D., Henning T., Helling C., Ilgner M., Sedlmayr E., 2003, A&A, 410, 611

Skinner M. A., Ostriker E. C., 2013, ApJS, 206, 21

Skinner M. A., Ostriker E. C., 2015, ApJ, 809, 187

Skinner M. A., Dolence J. C., Burrows A., Radice D., Vartanyan D., 2019, ApJS, 241, 7

Smith N., 2014, ARA&A, 52, 487

Smith A., Kannan R., Tsang B. T. H., Vogelsberger M., Pakmor R., 2020, ApJ, 905, 27

Stone J. M., Mihalas D., Norman M. L., 1992, ApJS, 80, 819

Su B., Olson G. L., 1996, J. Quant. Spectrosc. Radiat. Transfer, 56, 337

Swesty F. D., Myra E. S., 2009, ApJS, 181, 1

Toro E. F., 1997, The HLL and HLLC Riemann Solvers. Springer Berlin Heidelberg, Berlin, Heidelberg, p. 293

Tsang B. T. H., Milosavljević M., 2015, MNRAS, 453, 1108

Tsang B. T. H., Milosavljević M., 2018, MNRAS, 478, 4142

Turk M. J., Smith B. D., Oishi J. S., Skory S., Skillman S. W., Abel T., Norman M. L., 2010, ApJS, 192, 9

Turner N. J., Stone J. M., 2001, ApJS, 135, 95

Turner N. J., Fromang S., Gammie C., Klahr H., Lesur G., Wardle M., Bai X. N., 2014, in Beuther H., Klessen R. S., Dullemond C. P., Henning T., eds, Protostars and Planets VI. Univ. Arizona Press, Tucson, p. 411

van der Holst B. et al., 2011, ApJS, 194, 23

Vaytet N. M. H., Audit E., Dubroca B., Delahaye F., 2011, J. Quant. Spectrosc. Radiat. Transfer, 112, 1323

Virtanen P. et al., 2020, Nature Methods, 17, 261

Wibking B. D., Krumholz M. R., 2021, preprint (arXiv:2110.01792)

Wolfire M. G., Cassinelli J. P., 1986, ApJ, 310, 207

Zel'dovich Y. B., Raizer Y. P., 1967, Physics of Shock Waves and High-Temperature Hydrodynamic Phenomena. Academic Press, New York

Zhang D., 2018, Galaxies, 6, 114

Zhang X., 2020, Res. Astron. Astrphys., 20, 099

Zhang W., Howell L., Almgren A., Burrows A., Bell J., 2011, ApJS, 196, 20

Zhao B. et al., 2020, Space Sci. Rev., 216, 43

APPENDIX A: HYPERBOLIC WAVESPEEDS FOR RADIATION SUBSYSTEM

A1 HLLE wavespeed correction

In this section, we demonstrate that our approach to estimating wavespeeds for describing the HLLE Riemann fluxes at cell interfaces produces the correct solution in the diffusion limit, and show why the wavespeed correction as described in Section 2.2.3 is necessary, especially with AMR. The fundamental issue is that using a maximum/minimum wavespeed (λ_{max}, λ_{min}) for the Riemann flux based on the characteristic speed obtained from the eigenvalues of the streaming limit radiation moment equation leads to a scheme that is too diffusive when the optical depth across a cell $\tau \gtrsim 1$. This is because the numerical diffusive flux due to the HLLE Riemann solver can be much larger than the physical radiative flux (Audit et al. 2002). To circumvent this issue, one can modify the wavespeed in a manner described in Section 2.2.3. We demonstrate below that this improves the solution considerably, even when the optical depth per cell is close to unity.

To demonstrate why wavespeed correction is necessary, we set up a problem identical to the weak equilibrium pulse test described in Section 3.1, without performing the wavespeed correction, for three different uniform grids of 256, 1024, and 4096 cells. For comparison, we also perform a version of the test at a resolution of 256 cells with the wavespeed correction enabled. Using the parameters of the test, the optical depths per cell with this setup are $\tau \approx 1.5$, 0.4, and 0.1, respectively for the three resolutions, making the cells only marginally optically thick. However, even in this case, we show in Fig. A1 that the solution without the wavespeed correction is significantly more diffusive, and only converges to the analytical solution when the photon mean free path is well resolved. On the other hand, we find that we can obtain similar accuracy at a resolution of 256 cells with the wavespeed correction. We note that the setup is only marginally optically thick, and the effect of the correction would be even larger at higher cell optical depths. The test above verifies that the wavespeed correction is a robust approach to obtain the right solution in the diffusion limit.

A2 Wavespeed correction at AMR level boundaries

We next demonstrate the generalization of our wavespeed correction to interfaces where the left and right cells have different widths (i.e. at level interfaces). As described in Section 2.2.3, for interfaces between cells at the same AMR level, we use the arithmetic average of the optical depth of the cells sharing the interface to compute the correction factor. On the other hand, for an interface at an AMR level boundary, where one neighbouring cell is finer than the other, we use the upstream value of the optical depth for the correction factor. To show why this change is necessary, we repeat the weak equilibrium diffusion pulse test of Section 3.1 with a base grid resolution of 1024 cells. We enforce a simple fixed refinement condition, refining the region $x < 0.5$ by a factor 2 in cell width, leaving the region $x > 0.5$ at the base resolution, which leads to a single level boundary in the domain. We perform four variations of the test for comparison – (i) without the HLLE wavespeed correction, (ii) using wavespeeds corrected with a correction factor computed from the arithmetic average optical depth at the interface, (iii) using wavespeeds corrected with a correction factor computed from the optical depth of the cell upstream to the wave propagation direction, and (iv) a uniform grid (UG) version of the problem where the entire domain is resolved by 2048 cells, corresponding to the resolution of the finer level of the AMR domain. We show the numerical solution we obtain for the radiation flux F_r for these four cases in Fig. A2, shading the region of the domain that is refined to a higher AMR level. We show only F_r as we found E_r to be relatively smooth for this test even with AMR, though in some other tests we found discontinuities at AMR levels in E_r as well.

We can clearly see from Fig. A2 that there is a sharp discontinuity at the level interface for the version without the wavespeed fix (AMRNoCorr). This discontinuity can be explained by the fact that the numerical diffusivity, which dominates over the physical diffusivity without the wavespeed correction, changes discontinuously across the coarse-fine interface, and this leads to a mismatch in the solution at the interface. The wavespeed correction using the average optical depth at the interface (AMRAverage) alleviates this discontinuity, but instead produces spurious oscillations near the interface. On
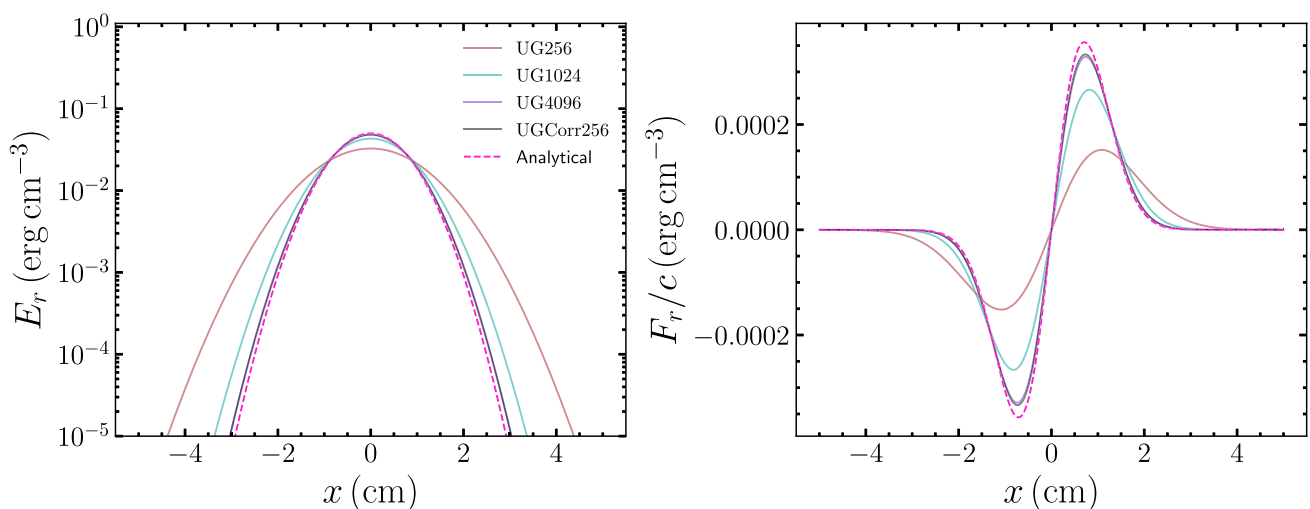
Figure A1. The numerical solution for the radiation energy (E_r) and flux (F_r) of the diffusing radiating pulse test of Section 3.1 obtained for a uniform grid (UG) with resolutions N_x (optical depth/cell τ) of 256 ($\tau \sim 1.5$), 1024 ($\tau \sim 0.4$), and 4096 cells ($\tau \sim 0.1$) without the HLLE wavespeed correction described in Section 2.2.3 (solid coloured lines), and that for a resolution of 256 cells with the wavespeed correction (solid black line). The dashed pink line shows the exact solution provided in Section 3.1. We see that the numerical solution is too diffusive without the wavespeed correction, and requires high resolution to converge to the right solution, whereas the version with wavespeed correction remains close to the right solution even at lower resolutions.
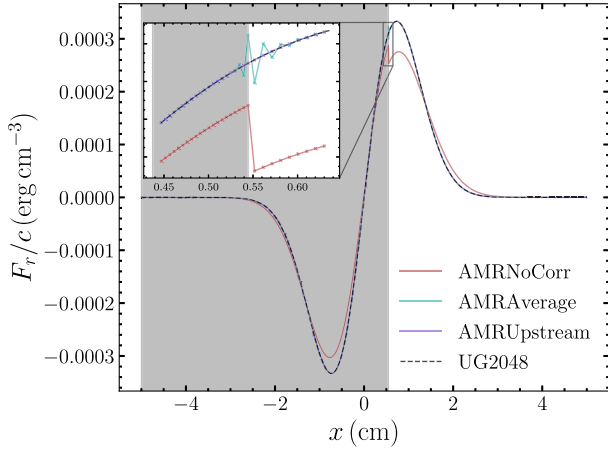
Figure A2. The numerical solution for the radiation flux (F_r) for the weak equilibrium diffusion test of Section 3.1 in a domain with a fine (shaded) to coarse (unshaded) AMR level boundary, with the fine cells at a resolution of $\Delta x \sim 0.0048$ cm and the coarse cells at $\Delta x \sim 0.0097$ cm. We show four variations of the test – (i) without the HLLE wavespeed correction described in Section 2.2.3 (AMRNoCorr), (ii) corrected wavespeeds using an arithmetic average optical depth at the interface for the correction factor (AMRAverage), (iii) corrected wavespeeds using the optical depth of the cell upstream to the wave propagation direction (AMRUpstream), and (iv) a uniform grid version with wavespeed correction at the resolution of the finer level of the AMR domain (UG2048). The inset zooms in the cells near the level interface to demonstrate the presence of discontinuities (oscillations) in the AMRNoCorr (AMRAverage) version. We can see that AMRUpstream version provides a smooth and accurate solution throughout the domain.

the other hand, using the optical depth of the upstream cell for the correction factor (AMRUpstream) leads to a smooth solution, and matches the solution obtained by the uniform grid at the finer AMR level grid resolution (UG2048). We also experimented with several other possible methods of choosing the optical depth at the interface of AMR level transitions, and found that the upstream version led to the best results.

APPENDIX B: DEPENDENCE ON ANGULAR RESOLUTION OF RAY TRACER

We derive the VET in our scheme from a ray-trace-based solution to the time-independent RT equation, and the accuracy of the VET depends on the accuracy of our ray-tracing method. The most important parameter that controls this accuracy is the angular resolution N_Ω, i.e. the number of discrete angles over which the transfer equation is solved. As outlined in Section 2.2.5, we use the HEALPix scheme to discretize the unit sphere into equal-area pixels, with a base resolution of 12 angular pixels, and further levels differing by a factor of 4 in the number of angles (i.e. $N_\Omega = 48$, 192, 768, ...). To evaluate the effects of varying N_Ω, we repeat the shadow test described in Section 3.8.2 with four different angular resolutions: 12, 48, 192, and 768 angles. We show the resulting temperature structures after a light crossing time of the computational box in Fig. B1. We find that all four angular resolutions produce reasonable temperature structures, but, as expected, the shadow becomes increasingly sharp with larger N_Ω; however, even for $N_\Omega = 48$ a clear umbra is visible. While the dependence on angular resolution will in general be problem-dependent, this comparison provides confidence that reasonable results can be obtained even with relatively modest angular resolutions.
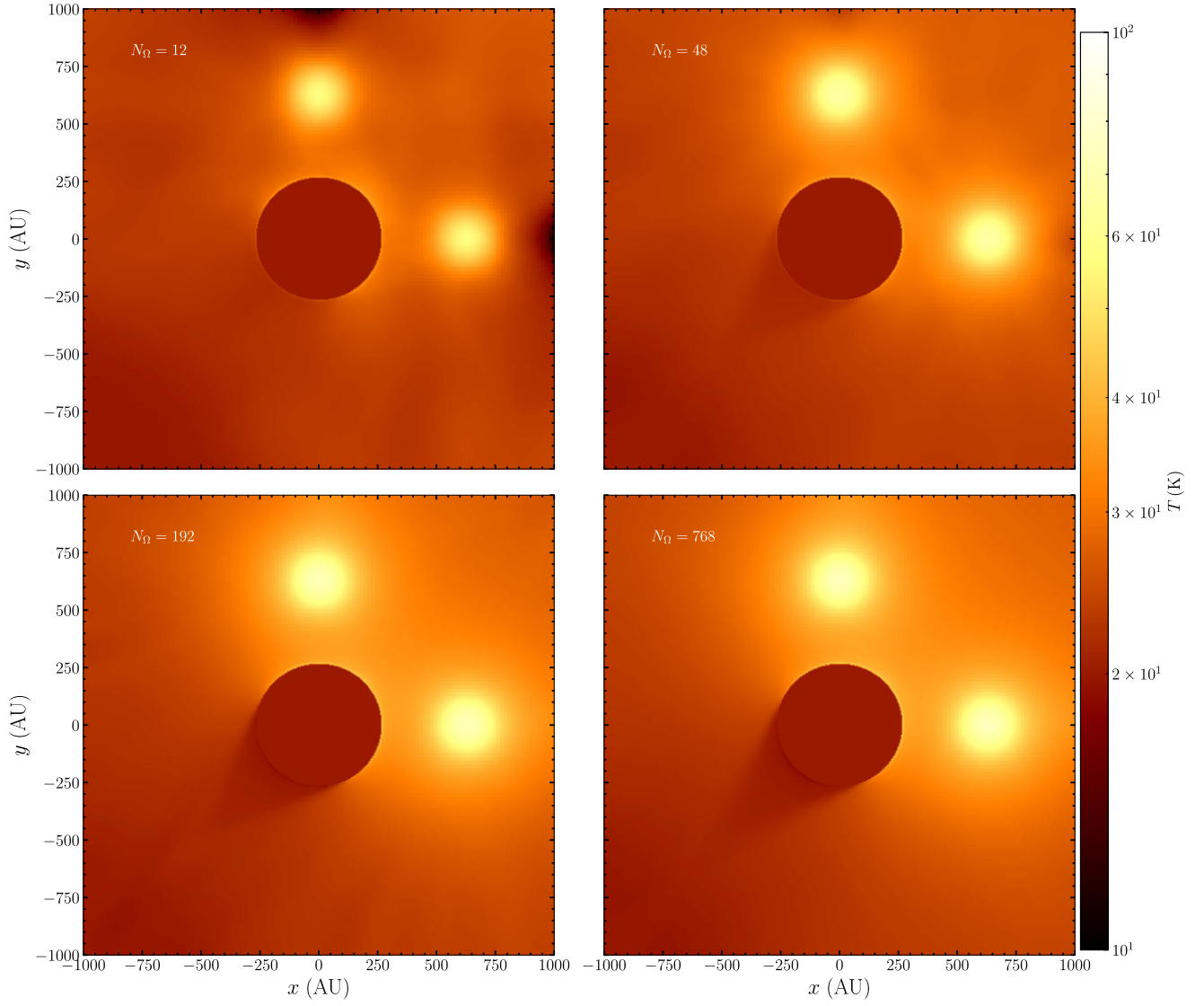
Figure B1. Comparison of the temperature structure obtained in the test described in Section 3.8.2 for varying numbers of angles (N_Ω) used in the ray tracer to compute the VET.

This paper has been typeset from a TEX/LATEX file prepared by the author.